A tri-channel oxide transistor concept for the rapid detection of biomolecules including the SARS-CoV-2 spike protein

Yen-Hung Lin[*,†], Yang Han[†], Abhinav Sharma, Wejdan S. AlGhamdi, Chien-Hao Liu, Tzu-Hsuan Chang, Xi-Wen Xiao, Wei-Zhi Lin, Po-Yu Lu, Akmaral Seitkhan, Alexander D. Mottram, Pichaya Pattanasattayavong, Hendrik Faber, Martin Heeney*[*], Thomas D. Anthopoulos**

Dr. Yen-Hung Lin, Prof. Thomas D. Anthopoulos
Blackett Laboratory, Department of Physics, Imperial College London, London SW7 2AZ, United Kingdom

Dr. Yen-Hung Lin
Clarendon Laboratory, Department of Physics, University of Oxford, Oxford OX1 3PU, United Kingdom
E-mail: yen-hung.lin@physics.ox.ac.uk

Dr. Yang Han, Prof. Martin Heeney
Department of Chemistry, Imperial College London, London SW7 2AZ, United Kingdom
Email: m.heeney@imperial.ac.uk

Dr. Yang Han
School of Materials Science and Engineering, Tianjin University, Tianjin 300072, China

Dr. Abhinav Sharma, Wejdan S. AlGhamdi, Akmaral Seitkhan, Dr. Hendrik Faber, Prof. Thomas D. Anthopoulos
King Abdullah University of Science and Technology (KAUST), KAUST Solar Centre, Thuwal 23955-6900, Saudi Arabia
E-mail: thomas.anthopoulos@kaust.edu.sa

Prof. Chien-Hao Liu, Xi-Wen Xiao, Wei-Zhi Lin, Po-Yu Lu
Department of Mechanical Engineering, National Taiwan University, Taipei 10617, Taiwan

Prof. Tzu-Hsuan Chang
Department of Electrical Engineering, National Taiwan University, Taipei 10617, Taiwan

Dr. Alexander D. Mottram, Dr. Pichaya Pattanasattayavong
Department of Materials Science and Engineering, School of Molecular Science and Engineering, Vidyasirimedhi Institute of Science and Technology (VISTEC), Rayong 21210, Thailand

Keywords: transistors sensors, metal oxide semiconductors, SARS-CoV-2, solution process, large-area electronics, solid-state devices

Abstract

Solid-state transistor sensors that can detect biomolecules in real time are highly attractive for emerging bioanalytical applications. However, combining upscalable manufacturing with the required performance remains challenging. Here we develop an alternative biosensor transistor concept that relies on a solution-processed In_2O_3/ZnO semiconducting heterojunction featuring a geometrically engineered tri-channel architecture for the rapid, real-time detection of important biomolecules. The sensor combines a high electron mobility channel, attributed to the electronic properties of the In_2O_3/ZnO heterointerface, in close proximity to a sensing surface featuring tethered analyte receptors. The unusual tri-channel design enables strong coupling between the buried electron channel and electrostatic perturbations occurring during receptor-analyte interactions allowing for robust, real-time detection of biomolecules down to attomolar (aM) concentrations. The experimental findings are corroborated by extensive device simulations, highlighting the unique advantages of the heterojunction tri-channel design. By functionalizing the surface of the geometrically-engineered channel with SARS-CoV-2 (Severe Acute Respiratory Syndrome Coronavirus 2) antibody receptors, we demonstrate real-time detection of the SARS-CoV-2 spike S1 protein down to aM concentrations in under two minutes in physiological relevant conditions.

Introduction

Miniaturised biochemical sensors fabricated via high-throughput manufacturing methods promise cost-effective, large-volume production for use in various technology sectors.[1] The present needs for biochemical detection are diverse and include environmental monitoring,[2] security systems,[3] and preventative medical care.[4] An ideal biochemical sensing platform should be able to accommodate a wide range of applications in biological and chemical detections with high-sensitivity[5] and selectivity.[6] Among the various types of sensing platforms, a solid-state transistor sensor is a highly-anticipated tool that could address these requirements as it provides the functionality of a transducer for converting a biochemical interaction into an amplified electrical signal.[7] This characteristic enables direct readout without the need of bulky peripheral driving (opto)electronics, such as amplifiers, excitation light sources and photo-detectors.[8]

For the successful use of solid-state transistors as biosensors, the transistor channel should exhibit a large surface area[9] and tuneable surface chemistry.[10] The large surface area allows tethering of sufficient quantity of molecular receptors while the surface helps to preserve charge transport across the channel without unintentionally reacting with the environment. One

widely reported biosensor technology platform is based on silicon-nanowire (Si-NW) transistors, but their manufacturing remains challenging.[11-13] Alternative technologies such as thin-film transistors (TFT) made of metal oxide semiconductors offer scalable manufacturing and intriguing physical properties.[14-17] However, due to parasitic gating effects and associated performance deterioration,[18-21] the use of metal oxide transistors as biosensors has remained limited with most effort focused on liquid-gated transistors (LGTs).[6, 22-24] In spite of being one of the most studied device, LGT biosensors face the detrimental Debye screening effect[6, 25-26] – a direct result of the operating principles that rely on electrochemical reactions[27] or on the movement of analytes[28] upon liquid-gating. Thus, managing or overcoming the Debye screening effect is critical for developing ultra-sensitive transistor sensor technologies for emerging applications.[29] Such technologies will largely benefit point-of-care systems in healthcare with the potential to mitigate existing challenges that include false results, long-waiting time, and the need for highly specialized equipment and trained staff.[30]

Here, we introduce a nanometres-thin In_2O_3/ZnO heterojunction channel and combine it with a geometrically engineered tri-channel architecture several millimetres in size as a universal platform for selective and sensitive biosensing. The all-solid-state device consists of a central sensing channel and two side channels featuring a buried electron transporting heterointerface a few nanometres below the channel's surface. The flexible surface chemistry of the metal oxide allows direct functionalisation of different types of receptors, making the device a versatile sensing platform. Despite being a thin-film transistor, the tri-channel architecture facilitates access to mm^2-size sensing surface without compromising the sensor's electrical performance due to its enhanced electron mobility and ultrahigh surface-area-to-volume ratio (10^6 cm^2 cm^{-3}). These features enable simultaneous signal transduction and amplification in an all-solid-state TFT platform, enabling real-time detection of specific biomolecules down to attomolar (aM) concentrations. As a proof-of-concept, we demonstrate selective sensing of the SARS-CoV-2 (Severe Acute Respiratory Syndrome Coronavirus 2) spike S1 protein in real-time with a limit of detection (LoD) of 865 aM in phosphate buffered saline (PBS) and <1 fM in human serum in less than two minutes.

Quasi-two-dimensional oxide heterojunction channel

We hypothesized that our recently developed solution-processed, high electron mobility In_2O_3/ZnO heterojunction (HJ) transistors[31] offers certain features that could prove attractive for biosensing. Firstly, the buried electron channel located at the oxide HJ is physically separated from the receptor units tethered on its surface a few nm above.[32-33] This feature is

expected to prevent degradation of electron transport upon sensing (e.g., due to Coulomb scattering) and preserve the transistor's performance. This is not the case for most biosensor transistors reported to date where the channel interacts directly with the receptor units and hence the analyte. To overcome this, liquid gating has been exploited for detecting various analytes in the liquid phase.[6, 22, 34] Secondly, the high electron mobility of the HJ TFTs offers the possibility for large electrical signals that are easy to detect and amplify even in large-size devices.[32]

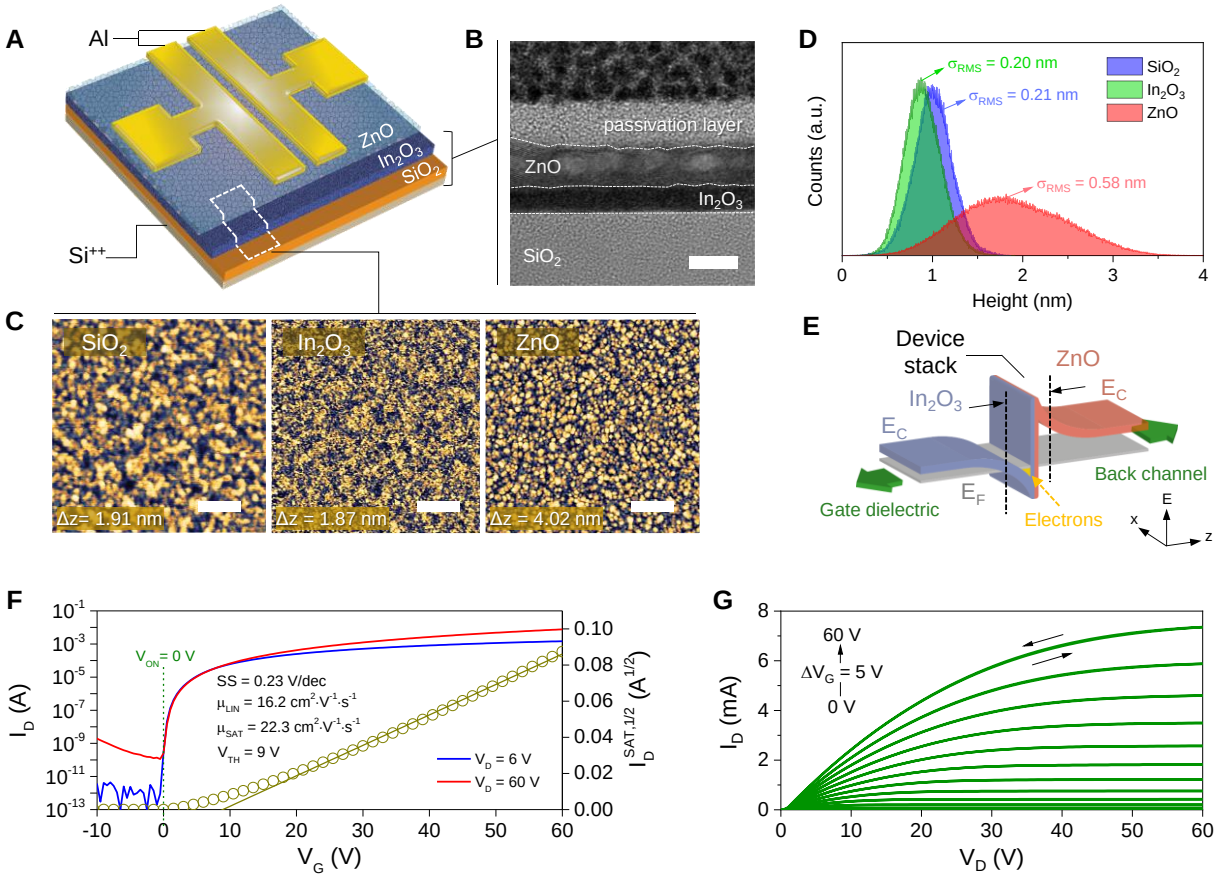

Figure 1. Fabrication and testing of metal oxide HJ transistors. (**A**) Schematic of an In_2O_3/ZnO HJ transistor. (**B**) HRTEM cross-sectional image of the channel region (scale bar = 5 nm). (**C**) Intermittent AFM topography images of SiO_2, In_2O_3 and ZnO surfaces (scale bar = 200 nm). (**D**) Height histogram extracted from the AFM data for each sequentially deposited layer. Corresponding peak-to-peak height difference (ΔZ) and root mean square surface roughness (σ_{RMS}) were derived from AFM image analysis. (**E**) Schematic of energetic diagram for the In_2O_3/ZnO heterointerface. The discontinuity in the conduction band between ZnO and In_2O_3 results to the electron migration from ZnO to In_2O_3. (**F** and **G**) Representative current-voltage (I-V) characteristics for a In_2O_3/ZnO transistor: (F) transfer and (G) output characteristics. Important device parameters are shown in (F). These include turn on voltage (V_{ON}), threshold voltage (V_{TH}), subthreshold swing (SS), linear mobility (μ_{LIN}), and saturation mobility (μ_{SAT}).

We fabricated HJ transistors using the staggered bottom-gate, top-contact (BG-TC) architecture shown in **Figure 1A**. High-resolution transmission electron microscopy (HRTEM) analysis (**Figure 1B**) of the channel reveals the formation of a well-defined HJ channel with thickness in the range of 8-10 nm. Atomic force microscopy (AFM) measurements show the existence of smooth layers as being deposited sequentially (**Figure 1, C** and **D)**. In_2O_3 exhibits the lowest peak-to-peak height (ΔZ) of 1.87 nm with a root-mean-square roughness (σ_{RMS}) value of 0.20 nm, which are comparable to that of SiO_2 (ΔZ = 1.91 nm, σ_{RMS} = 0.21 nm). Subsequent deposition of ZnO atop In_2O_3 leads to a slightly rougher topography (ΔZ = 4.00 nm, σ_{RMS} = 0.58 nm) indicative of a more textured surface.[32, 35]

The In_2O_3/ZnO forms a type-II HJ where electrons migrate from the conduction band (CB) of ZnO to that of In_2O_3, leading to the accumulation of electrons in the latter and in close proximity to the heterointerface (illustrated in **Figure 1E**).[33] We note that our actual device stack is low dimensional (**Figure 1B**) and as such it is difficult to probe with high enough accuracy (resolution) the change in the gradient of electron density distribution across the hetero-oxide interface where the higher density of electrons reside. From our modelled In_2O_3/ZnO channel (**Figure S1**) using the COMSOL Multiphysics® simulation software (see *Experimental*), the heterointerface might appear having a uniform electron distribution (**Figure S1C**). However, this observation is simply the result of the low dimensionality of the transistor channel and closer examination of the data reveals a clear gradient in electron density across the In_2O_3/ZnO heterointerface (**Figure S1**, **A**-**B**) in agreement with earlier experimental observations.[33] To make this feature more visible we highlighted the relative position of the In_2O_3/ZnO stack in **Figure 1E**. In **Figure 1**, **F** and **G**, we show representative sets of transfer and output current-voltage (I-V) characteristics for a In_2O_3/ZnO HJ transistor with electron mobility and current on-off ratio of >22 $cm^2\ V^{-1}\ s^{-1}$ and $>10^8$, respectively.

All solid-state tri-channel transistor sensor

To investigate the suitability of the In_2O_3/ZnO transistors for biosensing, we fabricated devices based on a tri-channel configuration on 4-inch Si wafers (**Figure 2A**). The source-drain (S-D) electrodes are deposited atop the In_2O_3/ZnO channel followed by the deposition of another ultrathin (2-4 nm) protective ZnO layer. Next the deoxyribonucleic acid (DNA) intercalator[36-37] 1-pyrenebutyric acid (PBA) was functionalised directly onto ZnO[38] acting as the DNA receptor. A second functionalisation step using butyric acid (BA) was also applied to ensure complete passivation of the ZnO surface (see the supplementary information and **Figure S2**).

The presence of BA helps to minimize the chemical interaction between the fluid (physiological or not) that is used to disperse the different analytes, and the surface of the SC (i.e. the upper ZnO layer). Importantly, the presence of BA does not affect the electronic characteristics of the device and hence it's sensing capabilities, which will be discussed later. The presence of PBA on the heterojunction channel was verified using ultraviolet–visible (UV-Vis) absorption measurements before and after functionalisation as evidenced by the appearance of distinct absorption peaks associated with the pyrene unit (**Figure S3**). The completed device consists of two identical 'conventional' channels (hereafter termed CC) 100 μm in length (L), formed on the sides, and a third long (L = 2000 μm) 'sensing' channel (hereafter termed SC) formed in the central region of the device between the S-D electrodes (see **Figure S4**). This unique channel layout offers a large sensing area channel where the analyte-containing solution can be easily applied while avoiding direct contact with the S-D electrodes (**Figure 2**, **B** and **C**) which is known to induce parasitic gating effects.[39]

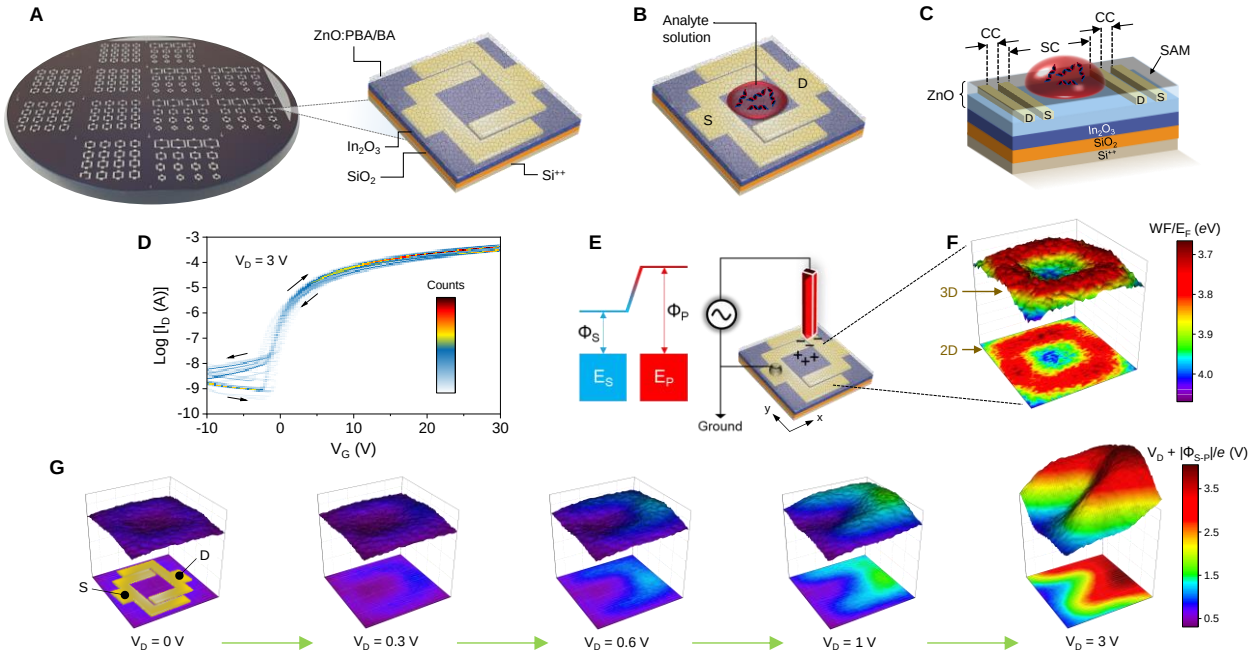

Figure 2. Design and structures of tri-channel transistor sensors. (**A**) Tri-channel In_2O_3/ZnO HJ transistors fabricated on a 4-inch Si^{++}/SiO_2 wafer and schematic of the channel architecture. The source-drain (S-D) electrodes are covered by the top ZnO layer. The receptor molecule pyrenebutyric acid (PBA) and passivation molecule butyric acid (BA) are chemically tethered onto the ZnO surface. The role of BA, which is deposited after PBA, is to prevent direct interaction between the channel's surface and the liquids used to disperse the various analytes. (**B**) Illustration of the direct application of analyte solution on the millimeter-scale sensing channel (SC) area of the sensor. (**C**) Schematic of the tri-channel transistor depicting the location of the analyte solution within the SC and two conventional channels (CCs) on the sides. (**D**) Density plots of forward-backward dual sweeps of current-voltage characteristics measured from 30 individual tri-channel transistor sensors fabricated on a wafer. (**E**) Schematic of the scanning Kelvin probe (SKP) setup used. The SKP method relies on the application of a voltage to offset

the surface potential between the sample (Φ_S) and the tip (Φ_P). The magnitude of this voltage is then used to calculate the energy difference between the sample (E_S) and the tip (E_P). (**F**) 2D (top)/3D (bottom) maps of the electrostatic potential across a tri-channel transistor measured by SKP. The WF for the embedded Al-electrode areas is measured to be ≈ 3.8 eV while the E_F for the SC is ≈ 4.0 eV. (**G**) Electrostatic potential maps measured at different source-drain potentials: V_D = 0, 0.3, 0.6, 1, and 3 V. The relative positions of the S-D electrodes are shown in the 2D map for V_D = 0 V.

In **Figures S5** and **S6**, we plot the transistor transfer and output characteristics, respectively, measured before and after PBA and BA functionalization. Unlike conventional transistor-based biosensors,[22, 40] our tri-channel device shows negligible changes in its operating characteristics following receptor functionalization. The narrow parameter distribution is better illustrated in **Figure 2D** which shows the density plots[41] of the dual-sweep transfer characteristics for 30 individual tri-channel transistors fabricated on a single wafer. Critically, the tri-channel transistors exhibit robust operation even when subjected to 90 repeated dual I-V sweeps with negligible leakage current (I_G) which is critical for optimal device operation and signal amplification (**Figure S7**).[42] We note that all devices were measured without any lightproof apparatus and under ambient atmosphere. These data demonstrate the high operational stability and reproducibility of the proposed tri-channel HJ transistor architecture.

To better understand the electrostatic potential landscape across the unconventional tri-channel device, we performed scanning Kelvin probe (SKP) measurements (**Figure 2E**). **Figure 2F** shows the two-dimensional (2D, bottom) and three-dimensional (3D, top) work function (WF) or Fermi energy (E_F) maps for a tri-channel device measured. The influence of the buried Al electrodes beneath ZnO results in local potential changes (3.8-4 eV), with a higher potential observed in the middle of the SC region. SKP measurements were also performed while applying a drain bias (V_D) in the range of 0-3 V (**Figure 2G**; the respective location of the device illustrated for V_D = 0 V image). The application of low voltages (e.g., V_D = 0.6-1 V) causes a substantial change within the SC, while increasing the applied bias to 3 V affects the potential landscape across the entire SC region, suggesting strong coupling between the SC and the two side CCs. Thus, the tri-channel architecture appears to enable spatially decoupling of the signal transduction occurring within the SC region from the current-driving CCs.

To understand how the tri-channel geometry impacts the electrical characteristics of the sensor, we built a simplified numerical model (**Figures S8-S9**) to simulate the electric potential distributions across the entire tri-channel device under a static state condition of V_G = 8 V and V_D = 3 V (**Figure S8A**). **Figure S8B** shows the modelled result in the presence of a circular-shaped analyte pattern (i.e. a realistic approximation of our sensing experiments), while **Figure**

S8C shows the data in the presence of a square shaped analyte pattern. In both cases the density of the modelled analyte was considered to be 3.3×10^{9} cm^{-2}. The square shaped analyte exhibits a stronger perturbation on the electrostatics of the device, when compared to circular shaped analyte. This phenomenon can be clearly observed in the presence of higher surface charge densities and in particular when increasing from 3.3×10^{9} to 6.7×10^{10} cm^{-2} (**Figure S9**). In all sensing scenarios, the electric potential gradient can readily reach the source-drain 90° corners for a square-shaped analyte whilst for a circular-shaped analyte area, the changes are relatively less apparent when reaching the 90° corners and appear mostly at the centre of the SC.

The calculated drain current obtained for **Figures S8A** (no analyte), **S8B** (a circular-shaped analyte) and **S8C** (a squared-shaped analyte) are 371, 377, and 383 μA, respectively. The excess currents of 6.2 and 11.5 μA for a circular- and a square-shaped analyte device, can then be obtained by subtracting the baseline current (i.e., no analyte) from the total current of the analyte-containing devices. The circular-shaped analyte device, which closely resembles the shape of a real-world analyte droplet, yields approximately ~50% less current than the square-shaped analyte device. Therefore, in our effort to study how the channel geometry affects charge flows, we utilised one half of a square-shaped analyte to model the influence of the analyte on the current-voltage characteristics of a tri-channel device in order to approximate the presence of a circular-shaped analyte. Further details are provided in the *Experimental* section. **Figure 3** shows the cross-sectional view along the centre of the tri-channel device (relative position indicated by the a and b arrows in **Figure S8B**). We can then simplify the geometric setting of the analyte by integrating each cross-section shown in **Figure 3** along the out of plane direction for one half of the length of an actual tri-channel device to obtain a current level close to the condition with the presence of a circular-shaped analyte.

Figure 3A shows the simulated and measured transfer characteristics for a representative transistor. The small difference seen in the subthreshold region between the modelled and experimental I-V data is attributed to the presence of trap states in the channel that are difficult to be captured, with high enough accuracy, by the model.[43-44] The slightly higher off current, on the other hand, measured for the real device is due to the combination of a large common Si^{++} gate electrode that was used in this study and the un-patterned layout of the semiconductor. The latter features are known to give rise to parasitic fringe surface currents forming between the S/D and the gate electrode, although in the presence case their contribution is very small (~0.1 nA) and hence negligible. Apart from these minor discrepancies, the model provides a good description of the tri-channel transistor operation and validates its ability to describe the operating characteristics of the sensor.

The main function of a transistor biosensor is to induce a perturbation in the channel current upon exposure to an external stimulus (analyte). To best illustrate this process in our sensor, we used the post-processing streamline tool for visualizing the electron concentration and the streamlines of the channel current flow. **Figure 3**, **B** to **F**, show the static distributions of the electron density and the streamlines of the current flow within the In_2O_3/ZnO heterostructure biased at V_D = 3 V and V_G = -1, 0, 1, 8 and 20 V. The results are in good agreement with our experimental observations and reveal the staggering enhancement in the current density within the In_2O_3 of the heterointerface.[32, 43] Next, we modelled the electrical characteristics of the device in the presence of an analyte. We hypothesize that the analyte species interacts with the surface-tethered receptor units and induce free charges at the surface of the SC region. To establish the sensing condition close to the limit of detection for our sensor, we assumed the number of additional charges induced by the analyte to be equivalent or lower than the number of mobile charges in the channel. Based on the literature,[45] as well as on our own work on similar heterojunction metal oxide channels,[32] device operation will remain largely unaltered when the additional electron concentration does not exceeds 10^{17} cm^{-3}.[35] To ensure that this condition is satisfied, we used a more conservative estimation for the analyte-induced electron density of 10^{16} cm^{-3} and a channel thickness of 10 nm (**Figure 1B**). The equivalent surface charge density due to analyte was then derived from the modelling yielding a value of $\approx 10^{10}$ cm^{-2}, which will be considered next for the different device operating scenarios.

Figure 3G shows the modelled transfer characteristics for a tri-channel (inset, **Figure 3G**) In_2O_3/ZnO sensor while **Figure S10** displays similar calculations for a single layer In_2O_3 and a In_2O_3/ZnO HJ transistors based on the conventional channel geometry (insets in **Figure S7**, **A** and **C**) before (baseline) and after exposure to analyte (analyte exposure). The tri-channel In_2O_3/ZnO transistor shows a large response to the analyte (surface charge $\approx 10^{10}$ cm^{-2}) with the transfer curve shifted towards more negative V_G bias. This is not the case for In_2O_3 and In_2O_3/ZnO transistors with conventional channel geometry (**Figure S10**, **B** and **D**), where the analyte induces only a small perturbation in the current around the subthreshold regime consistent with filling of sub-gap states.[46] The modelled electron density and current flow for the tri-channel transistor biased at V_D = 3 V and V_G = -1, 0, 1, 8 and 20 V, are presented in **Figure 3**, **H** to **L**, while the corresponding modelling results for the conventional channel In_2O_3 (at V_D = 3 V, V_G = 1 V) and In_2O_3/ZnO (at V_D = 3 V, V_G = -1 and 1 V) transistors are shown in **Figure S11**, **A** and **B**, and **Figure S11**, **C** to **F**, respectively. Strikingly, we find that unlike geometrically engineered In_2O_3/ZnO HJ transistors (**Figure 3**, **H** to **L**), electron flow in the In_2O_3 device is pinned at the interface with the gate dielectric while being fully decoupled from

the surface/analyte (**Figure S11B**). From these data we conclude that the tri-channel design is highly sensitive to the presence of surface charges as compared to conventional channel design, while single layer In_2O_3 transistors are not ideal for solid-state biosensing applications.

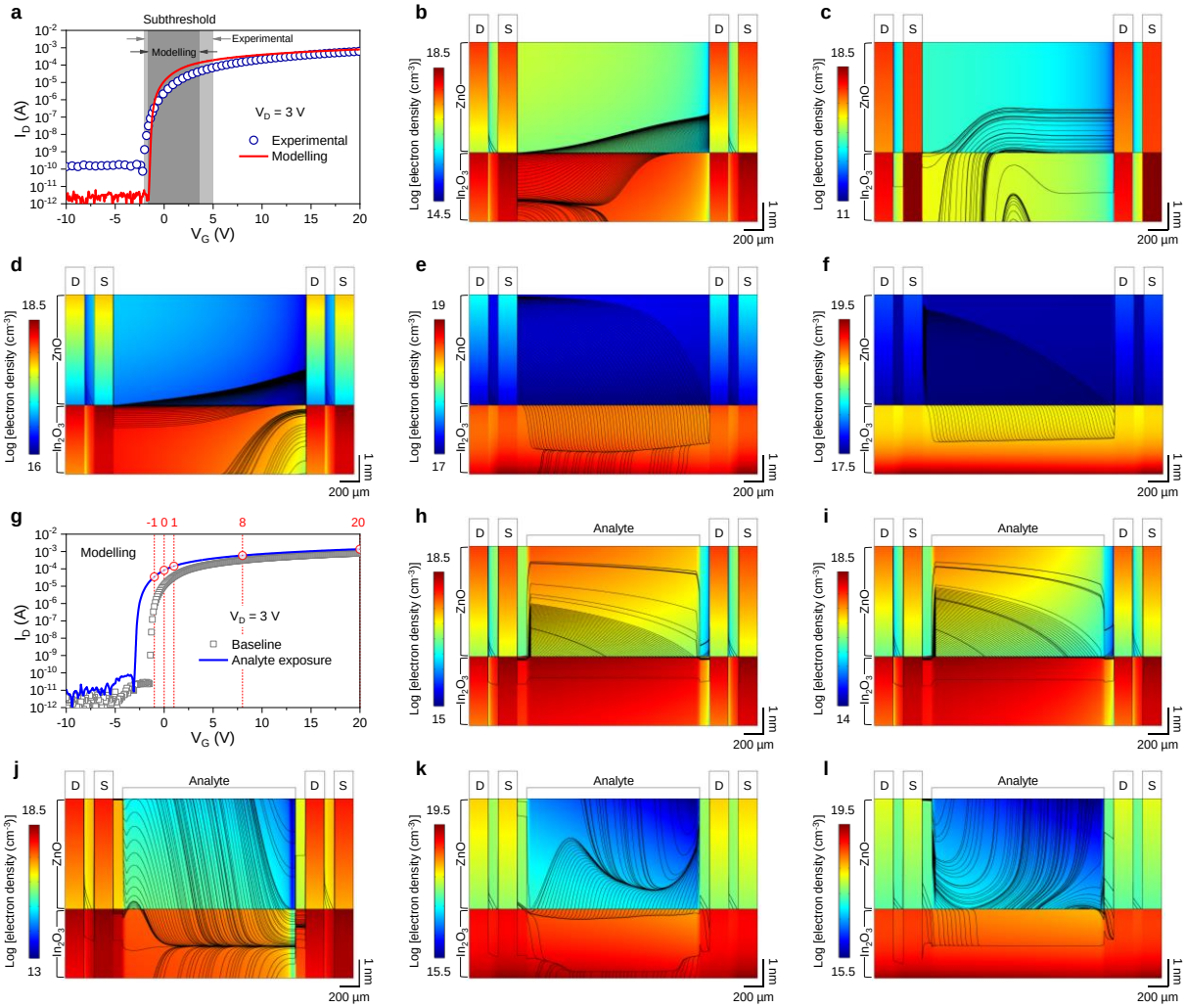

Figure 3. Physical principles of tri-channel transistor sensors. (**A**) Transfer current-voltage characteristics of tri-channel transistor sensors obtained from experiment and modelling using COMSOL Multiphysics®. The applied drain voltage (V_D) was +3 V, and the subthreshold regions are indicated in grey. (**B** to **F**) Corresponding COMSOL simulations showing the electron density distributions along the cross-section of the In_2O_3/ZnO heterostructure under the source and drain electrodes (labelled as S and D, respectively) and the electron flow streamlines within the channel regions, with different gate voltages (V_G) applied: (B) -1 V; (C) 0 V; (D) 1 V; (E) 8 V; (F) 20 V, and a constant V_D = 3 V. (**G**) Modelled transfer current-voltage characteristics (V_D = 3 V) for baseline and under the exposure of simulated surface-charged analytes. (**H** to **L**) Corresponding COMSOL electron density distributions under the influence of simulated analytes when applying V_D = 3 V and V_G = (H) -1 V; (I) 0 V; (J) 1 V; (K) 8 V; (L) 20 V to the transistor sensors. The electrodes and analytes are shown to indicate their positions with respect to the devices.

Next, we consider the scenario where the In_2O_3/ZnO HJ transistors are operated in depletion (V_G = -1 V) and in the presence of analyte (i.e., additional ≈10^{10} cm^{-2} on the SC surface). Clear perturbations in the current flow are observed for both tri-channel In_2O_3/ZnO

(**Figure 3**, **H** to **L**) and conventional channel In_2O_3/ZnO (**Figure S11**, **D** and **F**) transistors. The broader distribution of streamlines seen in the tri-channel is consistent with the large negative shift in the turn-on voltage (V_{ON}) of the device (**Figure 3G**). Regardless of the biasing scenarios (depletion or accumulation), the tri-channel architecture shows much stronger coupling to the analyte. Specifically, we find the electron flow streamlines to extend ≈1 nm beneath the SC surface (**Figure 3**, **H** to **L**) due to the asymmetric design of the source-drain electrodes,[47] which prevent the local electric field to fully pinch-off the channel at lower V_G biasing. As the V_G increases (e.g., +20 V), the benefits associated with the presence of a higher electron density in the In_2O_3/ZnO become even more apparent as the area beneath the sensing surface remains free from electrostatic screening induced by the gate (**Figure 3L**). Nevertheless, it is known to be more advantageous for solid-state transistor sensors to be operated within the subthreshold region as it yields optimal sensitivity due to the higher signal gain.[48]

To further highlight the key role of the side CCs, we carried out additional simulations on conventional single channel architectures and compared the results against those obtained for tri-channels, focusing on how the CCs perturbs the electric field and re-distributes the charges within the semiconducting heterojunction under similar biasing condition (V_G = V_D = 3 V). To make our simulation more perceivable, the length of the SC in the lateral direction (i.e., parallel to the gate dielectric) was reduced by a factor of 2×10^3 whilst the CC and top electrodes were reduced by a factor of 10^3 (**Figure S12**). We then assumed a low surface charge density of 5×10^9 cm^{-2} as the modelled analyte to examine how the CCs enhances the ability of the device to detect minute perturbations caused by the analyte-receptor interactions during sensing. As shown in **Figure S12A**, in regions 1 (i.e., areas highlighted by red dashed squares), the conventional single channel design (top) shows a significantly larger pinched-off region than the tri-channel device (bottom), whist in regions 2 (i.e., areas highlighted by black dashed squares), the tri-channel design (bottom) is able to sustain a significantly higher electron concentration within the SC. These observations highlight the key role of CCs in helping induce a stronger electric field, unpinning the channel current under the drain electrode of the SC and enhancing the electron extraction under the source electrode in the SC region. **Figure S12B** shows the corresponding electric field distributions across the conventional channel (top) and the tri-channel (bottom) architecture, further corroborating the proposed mechanism and the key role of the CCs. Importantly, the simulations protocol developed here can be seen as a powerful predictive tool that in the future could be exploited to further advance the tri-channel sensor design and lead to improved sensor capabilities.

Receptor engineering for ultra-sensitive and real-time biosensing

To demonstrate that the working principle of our all-solid-state tri-channel transistor is fundamentally different from that of conventional liquid-gate transistor biosensors, we studied the ability of our transistors to detect different types of DNAs (analytes) dispersed in deionized (DI) water rather than in a high ionic strength (and hence electrically conductive) solution often used in LGT sensors.[6] In the latter case, the high strength ionic medium (electrolyte, buffer solution etc.) represents an essential component as it facilitates the movement of charged species (or charges) which in turn "gate" the sensor's electrical signal (channel current).[6, 22-24] In contrast, the operation of the solid-state tri-channel sensor developed here does not rely on such electrochemical processes since sensing stems purely from the electronic interactions occurring between the surface tethered receptors (i.e. PBA) and the analyte species (i.e. DNA). To prove this, double-stranded DNA (dsDNA) and single-stranded DNA (ssDNA) of different sequences, were dispersed in DI-water solutions and applied directly onto the SC area while recording the device's electrical response. **Figure 4A** depicts the envisioned interaction between dsDNA and PBA where the pyrene units on PBA intercalate into the dsDNA.[49] **Figure 4**, **B** to **D** show the measured transfer characteristics (V_D = 3 V) in the presence of different concentrations of 20 base-pair segments of synthetic DNAs based on single-stranded adenine (A) [abbreviated as A20], and thymine (T) [abbreviated as T20], as well as their complementary dsDNA (AT)20. For (AT)20, a much larger change in the transistor's transfer characteristics is observed with the lowest dsDNA concentrations studied down to 100 aM (**Figure 4B**). The strong response is attributed exclusively to the intercalation of the pyrene units into the minor grooves of the double-stranded (AT)20 since the presence of DI water has no measurable effect (**Figure S13**). The progressive shift of V_{ON} towards more negative V_G seen in **Figure 4B** is consistent with the modelling results of **Figure 3G** where we considered the presence of additional free charges on the surface of the SC. This observation indicates that pyrene-NDA association generates free electrons that are then injected into the channel. Further evidence supporting our hypothesis comes from sensing experiments involving the single-stranded A20 (**Figure 4C**) and T20 (**Figure 4D**) where only minute changes are observed in the transistors' characteristics due to the absence of pyrene-DNA intercalation.

In an effort to quantify the sensor's response, we analysed the change in V_{ON} as a function of increasing analyte concentration. This shift reflects the increase in the electron concentration (Δe_{areal}) within the channel and is given as[50]

$$\Delta e_{areal} = \frac{C_{areal}[V_{ON}(conc.) - V_{ON}(init.)]}{q} \quad (1)$$

where C_{areal} is the areal capacitance of the gate dielectric (34.4 nF cm^{-2}), q is the elementary charge, V_{ON}(init.) is the initial V_{ON} measured in the presence of blank solution (no analyte), and V_{ON}(conc.) is the transistor's V_{ON} measured upon application of the analyte at each concentration. For simplicity, we assume all electrons are confined in a two-dimensional plane at the vicinity of the oxide HJ.[33] **Figure 4E** shows the evolution of Δe_{areal} as a function of analyte concentration measured using a tri-channel sensor. (AT)20 induces the highest Δe_{areal}, a direct consequence of the large V_{ON} shift observed in **Figure 4B**. These results demonstrate unambiguously that pyrene-(AT)20 intercalation produces signals several orders of magnitude larger than the non-intercalating ssDNAs of A20 and T20. Moreover, the data showcase the ability of the tri-channel sensor to differentiate between double and single stranded DNAs without the need for complex fluorescence labelling.[51] To this end, the DNA conformation with respect to the substrate (i.e., lying-down or standing up), should not be critical as sensing relies exclusively on the charge transfer upon pyrene-DNA association. This hypothesis is corroborated by the sensor's ability to selectively detect different analytes, such as avidin and SARS-CoV-2 spike S1 protein, which will be discussed latter. The ability of our sensor to facilitate such a strong coupling between the minute receptor-analyte interactions and charge transport, without compromising the channel transconductance (g_m) (see supplementary text and **Figure S14**), is a result of three unique device attributes:

i. The geometrical engineered tri-channel design that enables strong coupling between current transport across the device and receptor-analyte interactions in the surface.
ii. The use of a high electron mobility heterojunction metal oxide semiconductor featuring a buried channel.
iii. The versatile surface chemistry and the electronic properties of the metal oxides employed.

Due to the diverse range of biosensor transistor technologies to date[5-6] there is currently no clear consensus on the important figures of merit that can be used to define the performance of such devices. Here we attempt to draw an analogy from the field of phototransistors, since both types of sensors act as transducers with a highly V_G-dependent response, and define two practical figures of merit namely the responsivity ($R_{analyte}$) and sensitivity ($S_{analyte}$) (Supplementary Information and **Figure S15**). We first investigated the suitability of our tri-channel biosensor TFTs for real-time sensing of (AT)20 at an extremely broad range of analyte concentrations (10^{-18} to 10^{-6} M), while simultaneously assessing the sensors' ability to operate in aqueous conditions[9, 52]. Specifically, we monitored the evolution of ΔI_D at V_G = -1 V and V_D = 3 V, as a function of time for different (AT)20 concentrations. The biasing condition were

chosen to maximise the sensor's response by operating it in the subthreshold region[48] (**Figure S16**). **Figure 4F** shows a representative real-time recording of $\Delta I_D/I_0$ (where $I_0 = 3.16\times10^{-8}$ A) for analyte concentrations in the range 10^{-18} to 10^{-6} M, where a clear response across the entire range is observed. Even at 100 aM of (AT)20, the tri-channel TFT shows a significant increase in ΔI_D by ≈ 30 times (**Figure 4G**) in less than 2 min. This represents the highest response signal reported to date for biosensing transistors, including liquid-gated devices[5-6, 24]. Importantly, the sensor's sensitivity can be tuned by the V_G as shown in **Figure S17** where the $S_{analyte}$ is plotted *vs*. (AT)20 concentration for different V_G (-1, 0, +1 V). Even at sub-optimal biasing conditions (i.e. V_G = 1 V), the measured I_D for 100 aM (AT)20 increases to 4.2 μA ($\Delta I_D \approx 2.8$ μA) which is ≈ 300% higher than the baseline signal ($I_0 \approx 1.4$ μA) (**Figure 4B**). The large ΔI_D indicates that the actual sensitivity of the tri-channel sensors is well below 100 aM. To this end, we note that in the literature the most frequently reported parameter is the LoD, which is determined by the minimum detectable signals that are often far from suitable for real-time monitoring [5-6, 40, 53].

To further demonstrate the capabilities of our ultra-high $S_{analyte}$ tri-channel sensor, we analysed the sensing kinetics using the linear form of the Langmuir adsorption isotherm[54],[55]. **Figure S18A** displays a series of such measurements taken from **Figure 4F** but replotted by setting the time (t) at which the different concentrations of analyte were applied, to 0 sec. **Figure S18B** shows a representative trace for 1 pM of (AT)20 where three different sensing stages can be distinguished:

i. Concentration-limited diffusion stage where an accelerated diffusion process takes place as the analyte concentration increases.
ii. Association of analyte with the tethered receptor moieties i.e. 'primary' sensing process.
iii. Dissociation of analyte-receptor complexes before reaching a thermodynamic equilibrium.

The rate of the 'primary' sensing process shown in **Figure S18B** is representative of a zero-order reaction and is independent of the analyte concentration or the method with which it is being applied. For each concentration, a distinct peak between association and dissociation stages is observed and attributed to the immobilization of analyte species by the tethered receptors.[56-58] Therefore, and regardless of the sensing method, the existence of two-phase kinetics relates solely to the association and dissociation stages. Using the high-fidelity sensing data from **Figure S18,** the equilibrium constant (K_{eq}) was calculated yielding values of $(5.88 \pm 0.03) \times 10^8$ M^{-1} (**Figure 4H**).

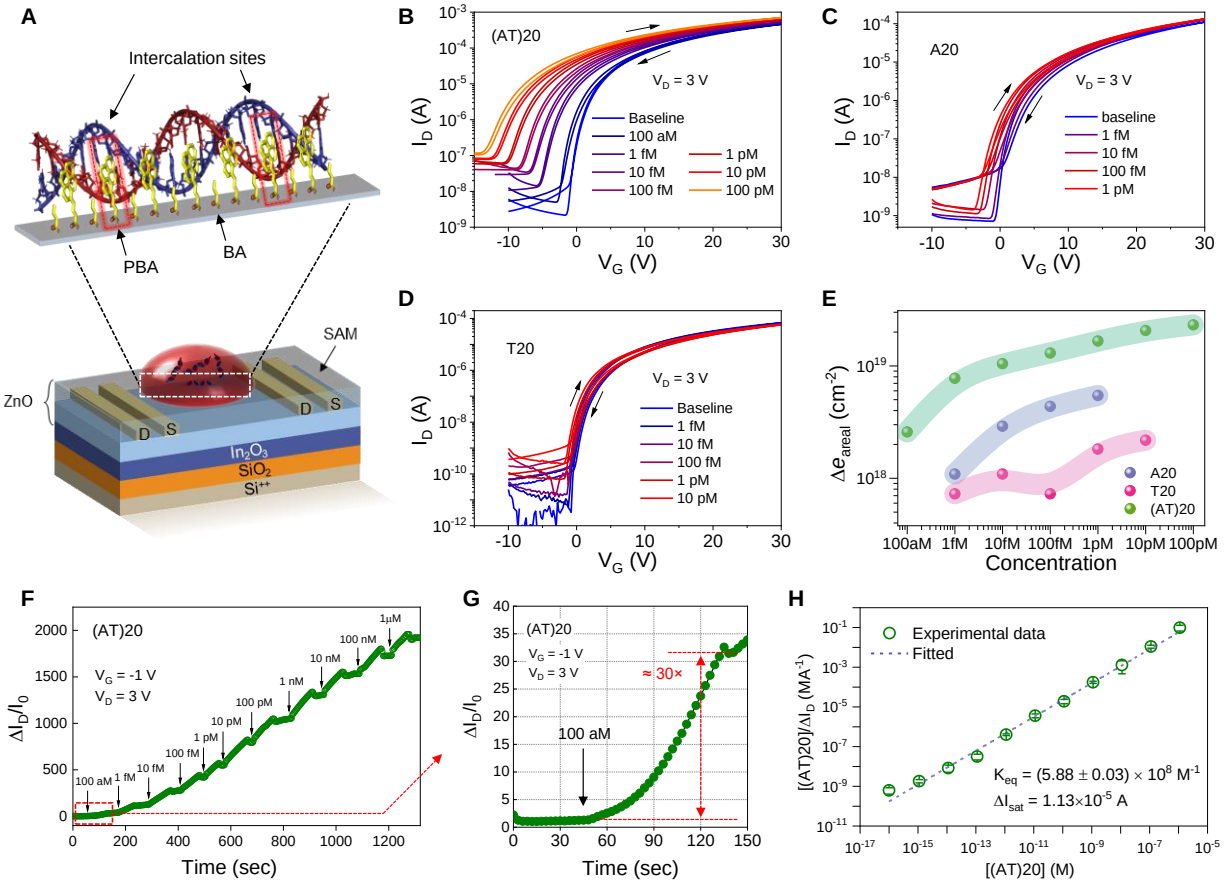

Figure 4. Tri-channel transistor sensor for synthetic DNA sensing. (**A**) Illustration of the envisioned intercalation between the pyrene units and dsDNA. (**B** to **D**) Transfer I-V characteristics (V_D = 3 V) measured from PBA/BA functionalised tri-channel transistor sensors with the presence of three types of DNA analytes: (B) (AT)20; (C) A20; (D) T20 at different analyte concentrations. (**E**) Plot of the increase in areal charge carriers Δe_{areal} that results from the sensing activity of the tri-channel transistor sensor to the analytes as a function of analyte concentration. Δe_{areal} is calculated from the shift in the turn-on voltage of the device upon the application of analyte solution. AT(20) shows the highest response due to its interaction via intercalation with pyrene units of the PBA-functionalised tri-channel transistor sensor. (**F**) Real-time response measured from a PBA/BA functionalised solid-state tri-channel transistor sensor operated at V_G = -1 V and V_D = 3 V upon exposure to synthetic (AT)20 with concentrations from 100 aM to 1 µM. (**G**) recorded response to 100 aM showing ≈30 times enhancement in I_D. The arrows indicate the time when the different analyte concentrations were applied to the SC area of the tri-channel transistor. (**H**) Fitting of experimental results of synthetic AT(20) sensing at different analyte concentrations according to the Langmuir adsorption isotherm. The error bars denote standard deviations from three real-time measurement sets.

In addition to short synthetic DNA, we have also tested natural dsDNA extracted from calf thymus tissue, which has much longer DNA sequences. **Figure 5**, **A** and **B**, respectively, show the transfer characteristics (V_D = 3 V) and real-time response recorded at fixed V_D = 3 V and V_G = -1 V (**Figure S19**, $I_0 = 2.63 \times 10^{-8}$ A). The response is similar to that recorded for (AT)20 indicating that the sensing mechanism remains identical for the natural dsDNA. Even when aM concentrations of the dsDNA is applied, the recorded signal ($\Delta I_D/I_0$) increases by

more than 100× (inset of **Figure 5B**), further corroborating the unprecedented sensitivity of the tri-channel sensor. When compared to (AT)20, the sensor exhibits stronger response to natural dsDNA with a higher binding constant K_{eq} of (8.71 ± 0.01) $\times 10^9$ M^{-1} (**Figure 5C**). This difference is attributed to the stronger interaction between the longer sequence of calf thymus DNA and the surface-tethered pyrene receptor.

We further investigated the possibility of sensing the formation of the positively charged biotin-avidin pair – an important complex for biochemical analysis.[59] For this sensing purpose, we functionalized the surface of ZnO with biotin, acting as the receptor, and then applied a DI-water based solution containing avidin (analyte) at different concentrations. **Figure 5D** reveals a systematic shift in V_{ON} of the transistors towards more positive V_G with increasing avidin concentration. This trend indicates a continuously reducing electron concentration in the channel due to the positively charged nature of avidin and its electron accepting character. **Figure 5E** shows real-time sensing of different concentrations of avidin. A higher voltage bias setting that used V_D = 3 V and V_G = 8 V (**Figure S20**, $I_0 = 1.89 \times 10^{-5}$ A) was employed to compensate for the depleted electron concentration in the channel (manifested as a positive shift in V_{ON}) due to the biotin-avidin association. Analysis of the binding constant between avidin and surface-immobilized biotin (**Figure 5F**), yields a K_{eq} of (1.73 ± 0.09) $\times 10^{10}$ M^{-1}. The latter is lower than that reported for free avidin-biotin pairs (10^{13}–10^{15} M^{-1})[60-61] – a result attributed to the likelihood of the smaller quantity of tethered biotin receptors. It is noticeable that although biotin-avidin is known to be one of the strongest biological pairs, the sensitivity of the avidin sensor is lower than that of the dsDNA one due to the low charge density associated with avidin. Therefore, the binding strength between the receptor and analyte species does not appear to determine the sensitivity of the tri-channel sensor.

To summarize, the sensing mechanism in our all-solid-state tri-channel transistor sensors is different to that of liquid-gated sensor platforms.[5-6, 22-28] The sensing process was successfully modelled by considering the generation of free charges on the SC's surface upon receptor-analyte association (**Figure 3**, **G** to **L**) and highlighted the strong coupling to the channel current. The higher gradients in the SC observed towards the HJ/analyte interface with a higher electron density highlights how majority carriers are introduced and transported across the device upon receptor-analyte interaction. Importantly, the sensor can be easily repurposed via receptor engineering to detect both negatively (DNAs) as well as positively charged analytes (biotin-avidin). In the case of biotin-avidin interaction the channel current was shown to reduce due to the electron accepting nature of the formed complex. Another key feature of our tri-

channel sensor is the large size SC and its ability to accommodate a high density of receptors, which enable dynamic sensing over an extraordinary wide range of analyte concentrations.

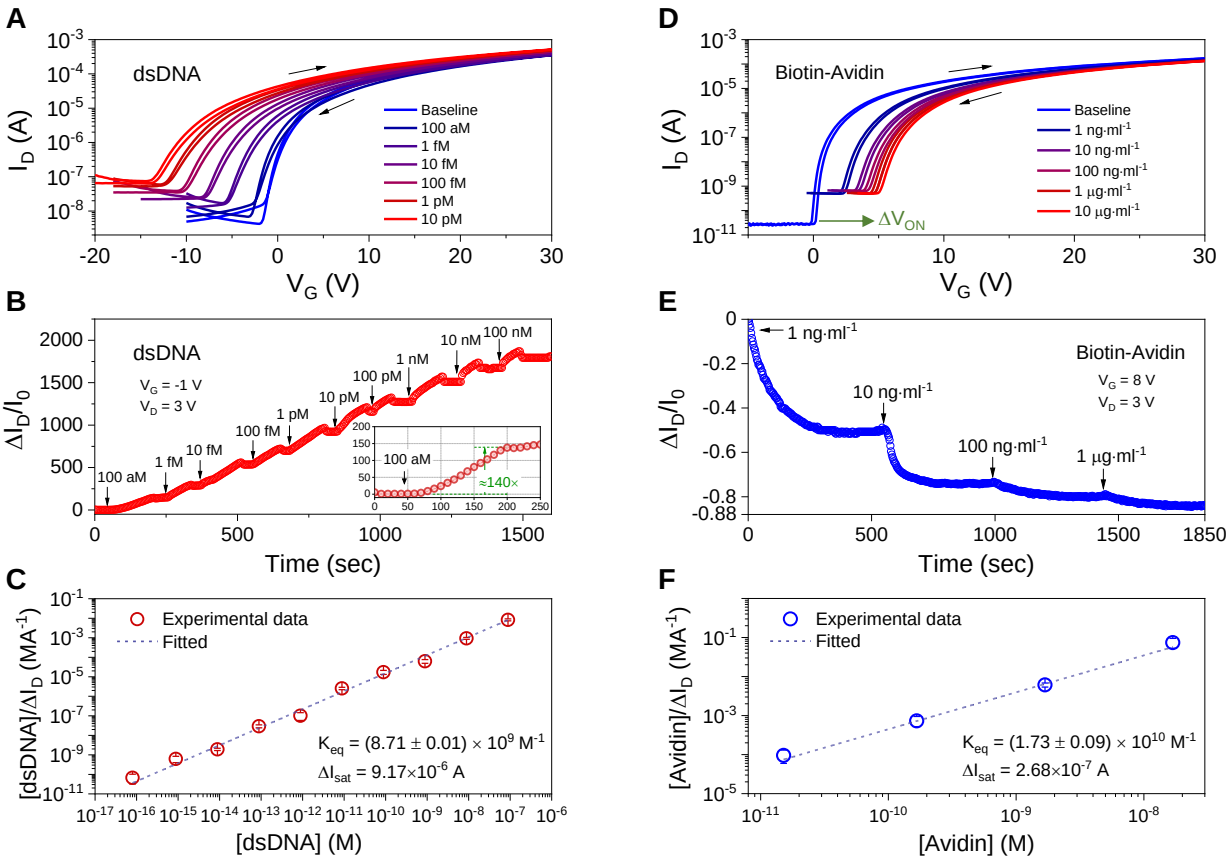

Figure 5. Attomolar detection of natural biomolecules. (**A**) Transfer characteristics (V_D = 3 V) of a PBA/BA functionalized tri-channel transistor sensor measured in the presence of natural dsDNA extracted from calf thymus. (**B**) Real-time response of a tri-channel transistor sensor to different concentrations (100 aM to 100 nM) of natural dsDNA. Inset: The sensor's response to a 100 aM of the analyte is ≈140 times higher than the baseline signal. For this experiment the device was operated at V_G = -1 V and V_D = 3 V. (**C**) Fitting of the experimental results for natural dsDNA at different analyte concentrations according to the Langmuir adsorption isotherm. The error bars denote standard deviations from three real-time measurement sets. (**D**) Transfer characteristics (V_D = 3 V) measured from a biotin-functionalized tri-channel transistor sensor subject to different concentrations of avidin. (**E**) Real-time response obtained from the biotin-based tri-channel transistor sensor biased at V_G = 8 V and V_D = 3 V. The avidin concentration was varied from 10 ng ml^{-1} to 1 µg ml^{-1}. The arrows indicate the time when the avidin was applied to the SC area of the sensor. (**F**) Fitting of experimental results of avidin sensing at different analyte concentrations according to the Langmuir adsorption isotherm. The error bars denote standard deviations from three real-time measurement sets.

Detection of SARS-CoV-2 spike S1 protein

To demonstrate the potential of the tri-channel transistors in a real-world sensing scenario, we engineered our devices by immobilizing SARS-CoV-2 antibody acceptors designed for specific binding to the SARS-CoV-2 spike S1 protein (**Figure 6A**).[53] The receptor-binding domain of the spike protein is known to bind the human cell receptor angiotensin-converting enzyme 2

(ACE2), followed by subsequent viral entry. During binding the positively charged polybasic cleavage site on the spike protein binds strongly with the negatively charged human cell receptor ACE2.[62] We hypothesized that such an interaction induces electrostatic perturbations that could become detectable by the tri-channel transistor.

To test our hypothesis, we first examined the ability of the sensor to operate under physiological-relevant conditions. The electrical characteristics of the antibody-tethered sensor show negligible change upon application of different concentrations of the high ionic strength phosphate buffered saline (PBS) solution directly onto the SC (**Figure S21** and **S22**). Next, a series of PBS solutions containing different concentrations of the SARS-CoV-2 spike S1 protein were prepared and applied onto the SC while the transfer characteristics of the sensor were recorded for each analyte concentration (**Figure 6B** and **Figure S23A**). A clear and systematic shift in V_{ON} towards more negative gate voltages with increasing analyte concentration, is observed. Strikingly, even at 10 aM the sensor's response remains large and clearly visible in the quasi-static transfer characteristics of **Figure 6B** indicating a high sensitivity.

To demonstrate the versatility of our tri-channel sensor platform, we performed real-time sensing measurements of the SARS-CoV-2 spike S1 protein. Prior to this, the tri-channel sensor was biased at V_G = -1 V and V_D = 3 V to acquire a baseline channel current of ≈1 μA ($\Delta I_D/I_0 = 0$). Following, PBS solutions containing varying concentrations of the SARS-CoV-2 spike S1 protein were applied sequentially to the SC while the sensor current being recorded in real-time (**Figure S23B**). Evidently, the sensor can detect the analyte across an ultra-wide range of concentrations (10 aM to 100 pM) demonstrating the tremendous potential of the technology. Similar to dsDNA real-time sensing measurements, the recorded signal ($\Delta I_D/I_0$) for each concentration increases and reaches an equilibrium followed by a small deep due to the diffusion limited, association and dissociation stages discussed previously.

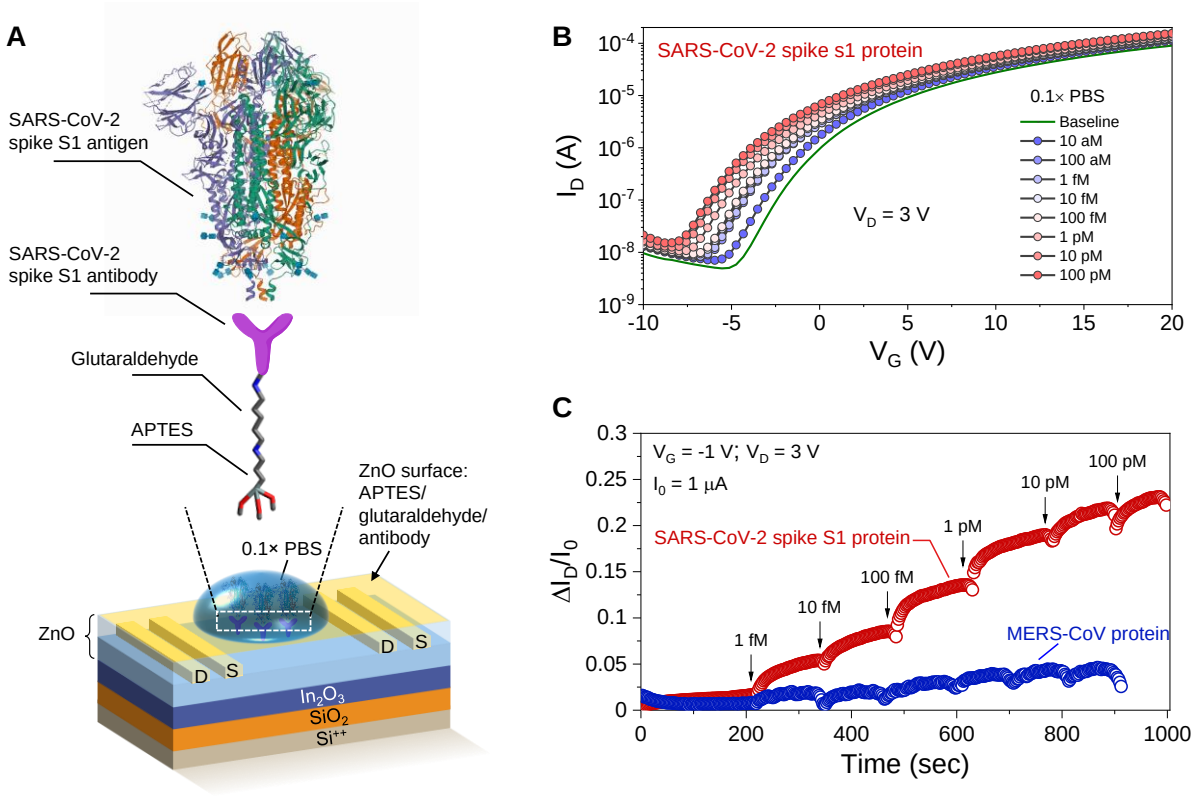

Figure 6. Detection of SARS-CoV-2 spike protein. (**A**) Schematic of the SARS-CoV-2 spike S1 protein detection. The SARS-CoV-2 spike S1 antibody is anchored onto the sensor platform after the sequential modification of oxide surface with 3-aminopropyltriethoxysilane (APTES) and glutaraldehyde. (**B**) Transfer characteristics (V_D = 3 V) of a fully functionalised tri-channel transistor sensor measured in the presence of the SARS-CoV-2 spike protein in 0.1× phosphate-buffered saline (PBS, baseline). (**C**) Real-time response of the tri-channel transistor sensors to different concentrations (1 fM to 100 pM) of the SARS-CoV-2 spike protein and the MERS-CoV protein in 0.1× PBS.

We have also examined the specificity of our sensor towards the SARS-CoV-2 spike S1 protein by comparing its real-time response against that of Middle East respiratory syndrome coronavirus (MERS-CoV) spike protein due to their genome similarities [63]. As can be seen in **Figure 6C,** the tri-channel sensor can differentiate between the two proteins under physiological relevant conditions. For the MERS-CoV protein, the sensor shows no response with the signal remaining largely unaltered with increasing analyte concentration from 1 fM to 100 pM. On the contrary, exposure to SARS CoV-2 spike S1 protein leads to a strong and systematic signal increase with increasing analyte concentration. The lowest concentration at which these differences are detectable can be deducted from **Figure 6C** yielding approximately 1 fM [53]. Finally, the LoD [64] was estimated by applying the International Union of Pure and Applied Chemistry (IUPAC) protocol [65] to the calibration plot for SARS-CoV-2 spike S1 protein in **Figure S23C** yielding a value of 865 aM.

Finally, we have examine the ability of our tri-channel sensor to detect the presence of the SARS-CoV-2 spike S1 protein directly in human serum (HS). **Figure S24A** displays the real-time response of the tri-channel sensor to 10-fold HS (control sample) and the same HS containing different concentrations of the SARS-CoV-2 spike S1 protein. Unlike the negligible response observed towards the blank 10-fold HS solution for up to 800 sec (blue symbols), the sensor exhibits a clear response to HS containing SARS-CoV-2 spike S1 protein down to 1 fM concentration in well under two minutes. Moreover, the sensor's response is linear across all studied concentrations with a coefficient of determination R^2 = 0.98 (**Figure S24B**). These results further showcase the tremendous potential of our tri-channel oxide sensors for use in rapid point-of-care diagnosis of COVID-19 and beyond.

Conclusion

We have developed simple-to-manufacture, millimetre-scale, all-solid-state metal oxide transistor sensors that can detect the presence of various biomolecules down to attomolar concentrations in real time while being operated under physiologically relevant environments. Our study highlights a new tri-channel concept that combines high sensitivity and a large dynamic range in an all-solid-state platform fully compatible of sensing liquid-phase analytes. The versatile surface chemistry of the metal oxide semiconductors employed allows for the incorporation of different receptor units (e.g., antibodies, enzymatic recognition elements, aptamers), which is anticipated to enable the detection of a broader range of biomolecules with high reliability, sensitivity and specificity. Furthermore, the ability to distinguish between negatively and positively charged biomolecules as well as between the SARS-CoV-2 and MERS-CoV spike proteins, under physiological relevant environments, showcases the universality of the sensing platform, which can be readily exploited for addressing most urgent and practical sensing applications.

Experimental Section

Preparation of metal-oxide precursors. ZnO and In_2O_3 precursor solutions were prepared by dissolving zinc oxide (99.99%; Sigma-Aldrich) in ammonium hydroxide (50% v/v; Alfa Aesar) at a concentration of 10 mg ml^{-1} and anhydrous indium nitrate (99.99%; Indium Corporation) in 2-methoxyethanol (99.8%; Sigma-Aldrich) at a concentration of 20 mg ml^{-1}, respectively. As-prepared solutions were then stirred rigorously at room temperature for 24 h before use. This process yielded clear transparent oxide precursor solutions.

Fabrication of low-dimensional oxide transistors. Heavily doped silicon (Si^{++}) wafers with a thermally grown SiO_2 top-layer (100 nm) were used as the common gate electrode and the gate dielectric, respectively. Prior to the semiconductor deposition, the substrates were sonicated in a solvent bath each lasting for ≈10 min in the following sequence: 1) deionised (DI) water with a Decon 90 detergent (5 vol%); 2) DI water; 3) acetone; 4) isopropanol. The solvent residue was dried with dry nitrogen over the substrate surface. As the last cleaning step, the substrates were exposed to ultraviolet (UV) ozone treatment for 10 min. The In_2O_3 ultra-thin film was deposited by carrying out spin-casting of the as-prepared precursor solution onto the Si substrates at 6000 rpm for 30 s in ambient air, followed by a post-deposition thermal-annealing process for 60 min at 200 °C in ambient air. The top ZnO layer was deposited with the same procedure as that for the In_2O_3 layer. Fabrication of the transistors (channel width/length = 1000/100 μm/μm) was completed with thermal evaporation of 40-nm thick Al top source and drain (S–D) electrodes through a shadow mask in high vacuum ($\approx 10^{-6}$ mbar).

Transistor characterisation. Electrical characterisation of transistors was carried out using three micro-positioners (EB-700, EVERBEING), a homemade probe station and an Agilent B2902A source/measure unit. We note that all the voltages and currents of transistors described in this work are referenced to the source contact electrode.

Self-assembled layer preparation and surface modification. To prepare the modified device for DNA sensing, firstly 1-pyrenebutyric acid (PBA, 97%; Sigma-Aldrich) solution (1 mg ml^{-1} in anhydrous tetrahydrofuran (THF)) was applied on the surface of the transistor for 30 min and thoroughly rinsed with THF and dried under nitrogen atmosphere. Butyric acid (BA, ≥99%; Sigma-Aldrich) solution (1 mg ml^{-1} in anhydrous THF) was then applied to the PBA modified surface for 30 min and thoroughly rinsed with THF and dried under nitrogen atmosphere. To prepare the modified device for avidin sensing, biotin (99%; Sigma-Aldrich) solution (0.8 mg ml^{-1} in anhydrous ethanol) was first applied on the surface of the transistor for 30 min and thoroughly rinsed with ethanol and dried under nitrogen atmosphere. BA was then applied to fully passivate the uncovered surface following the same procedures above as for DNA sensor devices.

Analyte preparation and sensing. Deoxyribonucleic acid from calf thymus (Type XV, Activated, lyophilised powder), avidin (lyophilised powder, ≥10 units/mg protein), A20, T20, (AT)20, were purchased from Sigma and used as received. All analytes were well dissolved in

MilliQ water (18.2 MΩ·cm/25 °C) to reach the desired concentration according to the solution preparation instruction provided by the supplier. For the sensing process, the analyte solution was constantly applied onto the sensing area, and the electrical properties of the sensor devices were then recorded. For the real time sensing, the channel current was monitored during the continuous and consecutive application of analyte solution of different concentrations onto the same sensor device.

Ultraviolet–visible spectroscopy measurements. The ultraviolet–visible (UV-Vis) transmission measurements were performed using a Shimadzu UV-2600 UV–Vis spectrophotometer. The samples were prepared on quartz substrates using the same deposition parameters described in the Methods section for oxide thin-film deposition and self-assembled monolayer formation.

High-resolution transmission electron microscopy measurement. The samples for high-resolution transmission electron microscopy (HRTEM) analysis were prepared using the focused ion beam processing technique. A gold-plated layer with thickness of 5 nm was coated on sample via sputtering before the sample preparation to make its surface more conductive. The HRTEM images were acquired at 300 kV by a FEI Titan G2 80–300 microscope equipped with a high-brightness Schottky-field emission electron source and a high-resolution Gatan imaging filter Tridiem energy-filter.

Atomic Force Microscopy measurement. Atomic force microscopy study was carried out in tapping mode using an Agilent 5500 atomic force microscope in ambient atmosphere. The approximate resonance frequency of the cantilever was 280 kHz and the force constant was 60 $N \cdot m^{-1}$.

Scanning Kelvin probe measurement. Scanning Kelvin probe investigations were carried out using a KP Technology system (model SKP5050/APS02) with a 1 mm tip. Scanning was achieved by taking an individual Kelvin probe (KP) measurement in one location and then moving the motorised stage to bring the sample in position for the next KP measurement. This was repeated until data was gathered in a grid pattern of 60×60 points, spanning an area of ca. 4 mm × 4 mm. For each point location the tracking feature built into the software made sure to keep the average tip-to-sample-distance constant. Additional drain bias in the range of 0 to 3 V was applied using a Keithley B2400 Source-Meter unit. The WF and E_F values were calculated

using Silver as the reference material. All measurements were carried out in ambient air at room temperature and relative humidity of ca. 25%.

Real-time sensing data analysis of (AT)20, natural dsDNA from calf thymus and avidin. To analyse the real-time response of the synthetic dsDNA (AT)20 (**Figure 4H**), natural dsDNA (**Figure 5C**) and avidin (**Figure 5F**), the sensing results at different analyte concentrations were fitted according to the linear Langmuir adsorption isotherm equation[52]: $C_{analyte}/\Delta I_D = C_{analyte}/\Delta I_{sat} + 1/\Delta I_{sat}K_{eq}$, where ΔI_{sat} is the estimated change of the saturated channel current upon increasing the concentration of analyte, and K_{eq} is the binding constant of analyte with its corresponding receptor.

Solution preparation and device fabrication for spike protein sensing experiments. 3-aminopropyltriethoxylsilane (APTES) solution (99%), glutaraldehyde solution (70% in H_2O), bovine serum albumin (BSA, A2153), phosphate buffered saline (PBS, pH 7.4, 10×) and human serum (H4522) were purchased from Merck. SARS-CoV-2 spike S1 antibody (40150-R007), SARS-CoV-2 (2019-nCoV) Spike S1-His Recombinant Protein (40591-V08B1), MERS-CoV Spike/S1 Protein (S1 Subunit, aa 1-725, His Tag) (40069-V08H) were purchased from Sino Biological (China). All chemicals were used as received without further purification. Stock solutions of spike proteins were prepared using nuclease-free water and further diluted to different concentrations in 0.1× PBS where necessary. For the SARS-CoV-2 spike protein sensing, the tri-channel transistors were first treated with UV-irradiation for 10 min, APTES solution (2 wt%) in toluene was pipetted onto the oxide surface and left for 15 min, followed by rinsing with toluene and annealing at 120 °C for 1 h. A glutaraldehyde (GA) linker was added to the terminal amino ($-NH_2$) groups of APTES using a solution of 0.8% GA in DI water for 10 min at room temperature, followed by rinsing with DI water and drying with compressed N_2 gas. The bovine serum albumin (BSA, 100 µg mL^{-1}) in PBS was added to the SC for 30 minutes to prevent the non-specific bindings of the channel surface, followed by rinsing with PBS. In the following, a concentration of 200 µg mL^{-1} of spike antibody solution was dropped onto the functionalised device and kept at room temperature for 5 h in order to immobilise the spike S1 antibodies via covalent bonding. To complete the immobilisation process, the devices were rinsed with 0.1× PBS to remove unbound antibodies. The human serum was filtered using 0.2 µM pore size Whatman syringe filter (6870-1302) and 10-fold diluted in 0.1× PBS for real sample analysis. The SARS-CoV-2 spike structure in **Figure 6A** was adopted from the PDB ID:6VYB [66].

Device modelling and simulations. Oxide transistor sensors were modelled and simulated using the semiconductor module in COMSOL Multiphysics. The material and device parameters used in the modelling in this work were adopted from our previous studies on the same materials[32, 67-68]. The cross-sectional model was constructed based on the actual device dimensions shown in **Figure S4**. The oxide semiconductors were modelled based on their material parameters taken from our previous reports[32-33, 69]. The In_2O_3/ZnO interface was modelled as a continuous quasi-Fermi-level heterojunction. The S-D electrodes were modelled as Ohmic contacts whilst the gate was modelled using the Thin Insulator Gate node, employing the same SiO_2 dielectric condition as the actual device stack. The analyte was modelled as equivalent surface charges. All the other boundaries were modelled as insulations, indicating no normal flux such as current and electric displacement filed. Due to the large aspect ratio of the ultrathin oxide structures, the mapped mesh was generated for the entire transistor channel area with fine rectangular meshes. The modelling data displayed in **Figures 3** and **S10-S12** are based on the condition along the a-b plane shown in **Figure S8B**, followed by integration along the c-d direction (**Figure S8B**) for half of the length of the SC region. This approach helps to overcome limitations associated with the desktop version of the COMSOL in solving high mesh densities based on the finite element analysis.

References

[1] N. Bhalla, P. Jolly, N. Formisano, P. Estrela, *Essays Biochem.* **2016**, *60*, 1-8.

[2] S. Rodriguez-Mozaz, M. J. Lopez de Alda, D. Barceló, *Anal. Bioanal. Chem.* **2006**, *386*, 1025-1041.

[3] Y. Engel, R. Elnathan, A. Pevzner, G. Davidi, E. Flaxer, F. Patolsky, *Angew. Chem. Int. Ed.* **2010**, *49*, 6830-6835.

[4] B.-U. Hwang, J.-H. Lee, T. Q. Trung, E. Roh, D.-I. Kim, S.-W. Kim, N.-E. Lee, *ACS Nano* **2015**, *9*, 8801-8810.

[5] E. Macchia, K. Manoli, B. Holzer, C. Di Franco, M. Ghittorelli, F. Torricelli, D. Alberga, G. F. Mangiatordi, G. Palazzo, G. Scamarcio, L. Torsi, *Nat. Commun.* **2018**, *9*, 3223.

[6] N. Nakatsuka, K.-A. Yang, J. M. Abendroth, K. Cheung, X. Xu, H. Yang, C. Zhao, B. Zhu, Y. S. Rim, Y. Yang, P. S. Weiss, M. N. Stojanović, A. M. Andrews, *Science* **2018**.

[7] M. J. Madou, S. R. Morrison, *Chemical Sensing with Solid State Devices*, Academic Press, 1989.

[8] N. Pires, T. Dong, U. Hanke, N. Hoivik, *Sensors* **2014**, *14*, 15458.

[9] E. Stern, J. F. Klemic, D. A. Routenberg, P. N. Wyrembak, D. B. Turner-Evans, A. D. Hamilton, D. A. LaVan, T. M. Fahmy, M. A. Reed, *Nature* **2007**, *445*, 519.

[10] I. Park, Z. Li, A. P. Pisano, R. S. Williams, *Nano Lett.* **2007**, *7*, 3106-3111.

[11] A. Agarwal, K. Buddharaju, I. K. Lao, N. Singh, N. Balasubramanian, D. L. Kwong, *Sens. Actuat. A-Phys.* **2008**, *145-146*, 207-213.

[12] Y. Huang, X. Duan, Q. Wei, C. M. Lieber, *Science* **2001**, *291*, 630-633.

[13] V. Krivitsky, M. Zverzhinetsky, F. Patolsky, *Nano Lett.* **2016**, *16*, 6272-6281.

[14] X. Yu, T. J. Marks, A. Facchetti, *Nat. Mater.* **2016**, *15*, 383.

[15] T. D. Anthopoulos, *Nat. Mater.* **2019**, *18*, 1033-1034.

[16] S. Li, M. Tian, Q. Gao, M. Wang, T. Li, Q. Hu, X. Li, Y. Wu, *Nat. Mater.* **2019**, *18*, 1091-1097.

[17] E. Fortunato, P. Barquinha, R. Martins, *Adv. Mater.* **2012**, *24*, 2945-2986.

[18] J. S. Park, J. K. Jeong, H. J. Chung, Y. G. Mo, H. D. Kim, *Appl. Phys. Lett.* **2008**, *92*, 072104.

[19] S. J. Kim, J. Jung, K. W. Lee, D. H. Yoon, T. S. Jung, S. R. Dugasani, S. H. Park, H. J. Kim, *ACS Appl. Mater. Interfaces* **2013**, *5*, 10715-20.

[20] J. Jung, S. J. Kim, D. H. Yoon, B. Kim, S. H. Park, H. J. Kim, *ACS Appl. Mater. Interfaces* **2013**, *5*, 98-102.

[21] J. Jung, S. J. Kim, K. W. Lee, D. H. Yoon, Y.-g. Kim, H. Y. Kwak, S. R. Dugasani, S. H. Park, H. J. Kim, *Biosens. Bioelectron.* **2014**, *55*, 99-105.

[22] H. Chen, Y. S. Rim, I. C. Wang, C. Li, B. Zhu, M. Sun, M. S. Goorsky, X. He, Y. Yang, *ACS Nano* **2017**, *11*, 4710-4718.

[23] J. Kim, Y. S. Rim, H. J. Chen, H. H. Cao, N. Nakatsuka, H. L. Hinton, C. Z. Zhao, A. M. Andrews, Y. Yang, P. S. Weiss, *ACS Nano* **2015**, *9*, 4572-4582.

[24] D. Ohayon, G. Nikiforidis, A. Savva, A. Giugni, S. Wustoni, T. Palanisamy, X. Chen, I. P. Maria, E. Di Fabrizio, P. M. F. J. Costa, I. McCulloch, S. Inal, *Nat. Mater.* **2019**.

[25] G. S. Kulkarni, Z. Zhong, *Nano Lett.* **2012**, *12*, 719-723.

[26] C.-H. Chu, I. Sarangadharan, A. Regmi, Y.-W. Chen, C.-P. Hsu, W.-H. Chang, G.-Y. Lee, J.-I. Chyi, C.-C. Chen, S.-C. Shiesh, G.-B. Lee, Y.-L. Wang, *Sci. Rep.* **2017**, *7*, 5256.

[27] L.-H. Pan, S.-H. Kuo, T.-Y. Lin, C.-W. Lin, P.-Y. Fang, H.-W. Yang, *Biosens. Bioelectron.* **2017**, *89*, 598-605.

[28] R. Elnathan, M. Kwiat, A. Pevzner, Y. Engel, L. Burstein, A. Khatchtourints, A. Lichtenstein, R. Kantaev, F. Patolsky, *Nano Lett.* **2012**, *12*, 5245-5254.

[29] C. Lubrano, G. M. Matrone, G. Iaconis, F. Santoro, *ACS Nano* **2020**, DOI: 10.1021/acsnano.0c07053.

[30] C. Ménard-Moyon, A. Bianco, K. Kalantar-Zadeh, *ACS Sens.* **2020**, *5*, 3739-3769.

[31] A. F. Paterson, T. D. Anthopoulos, *Nat. Commun.* **2018**, *9*, 5264.

[32] H. Faber, S. Das, Y.-H. Lin, N. Pliatsikas, K. Zhao, T. Kehagias, G. Dimitrakopulos, A. Amassian, P. A. Patsalas, T. D. Anthopoulos, *Sci. Adv.* **2017**, *3*, e1602640.

[33] Y.-H. Lin, H. Faber, J. G. Labram, E. Stratakis, L. Sygellou, E. Kymakis, N. A. Hastas, R. Li, K. Zhao, A. Amassian, N. D. Treat, M. McLachlan, T. D. Anthopoulos, *Adv. Sci.* **2015**, *2*, 1500058.

[34] K. M. Cheung, K.-A. Yang, N. Nakatsuka, C. Zhao, M. Ye, M. E. Jung, H. Yang, P. S. Weiss, M. N. Stojanović, A. M. Andrews, *ACS Sens.* **2019**.

[35] S. P. Schießl, H. Faber, Y.-H. Lin, S. Rossbauer, Q. Wang, K. Zhao, A. Amassian, J. Zaumseil, T. D. Anthopoulos, *Adv. Mater.* **2016**, *28*, 3952-3959.

[36] N. Cho, S. A. Asher, *J. Am. Chem. Soc.* **1993**, *115*, 6349-6356.

[37] S. Laib, A. Krieg, P. Hafliger, N. Agorastos, *Chem. Commun.* **2005**, 5566-8.

[38] E. Tang, G. Cheng, X. Ma, X. Pang, Q. Zhao, *Appl. Surf. Sci.* **2006**, *252*, 5227-5232.

[39] I. Heller, A. M. Janssens, J. Männik, E. D. Minot, S. G. Lemay, C. Dekker, *Nano Lett.* **2008**, *8*, 591-595.

[40] J. Kim, Y. S. Rim, H. Chen, H. H. Cao, N. Nakatsuka, H. L. Hinton, C. Zhao, A. M. Andrews, Y. Yang, P. S. Weiss, *ACS Nano* **2015**, *9*, 4572-4582.

[41] M. El Abbassi, S. Sangtarash, X. Liu, M. L. Perrin, O. Braun, C. Lambert, H. S. J. van der Zant, S. Yitzchaik, S. Decurtins, S.-X. Liu, H. Sadeghi, M. Calame, *Nat. Nano.* **2019**, *14*, 957-961.

[42] S. Lee, A. Nathan, *Sci. Rep.* **2016**, *6*, 22567.

[43] Y.-H. Lin, W. Li, H. Faber, A. Seitkhan, N. A. Hastas, D. Khim, Q. Zhang, X. Zhang, N. Pliatsikas, L. Tsetseris, P. A. Patsalas, D. D. C. Bradley, W. Huang, T. D. Anthopoulos, *Nat. Electron.* **2019**, *2*, 587-595.

[44] X. Wang, L. F. Register, A. Dodabalapur, *Phys. Rev. Appl.* **2019**, *11*, 064039.

[45] T. Kamiya, K. Nomura, H. Hosono, *Sci. Technol. Adv. Mater.* **2010**, *11*, 044305.

[46] J. Raja, K. Jang, N. Balaji, W. choi, T. T. Trinh, J. Yi, *Appl. Phys. Lett.* **2013**, *102*, 083505.

[47] X. Liu, K. Yang, A. Wadhwa, S. Eda, S. Li, J. Wu, *Sens. Actuat. A-Phys.* **2011**, *171*, 406-413.

[48] X. P. A. Gao, G. Zheng, C. M. Lieber, *Nano Lett.* **2010**, *10*, 547-552.

[49] S. Laib, A. Krieg, P. Häfliger, N. Agorastos, *Chem. Commun.* **2005**, 5566-5568.

[50] Y. H. Lin, H. Faber, S. Rossbauer, T. D. Anthopoulos, *Appl. Phys. Lett.* **2013**, *102*, 193516.

[51] K. Matsumoto, Y. Shinohara, S. S. Bag, Y. Takeuchi, T. Morii, Y. Saito, I. Saito, *Bioorganic & Medicinal Chemistry Letters* **2009**, *19*, 6392-6395.

[52] E. Stern, A. Vacic, N. K. Rajan, J. M. Criscione, J. Park, B. R. Ilic, D. J. Mooney, M. A. Reed, T. M. Fahmy, *Nat. Nano.* **2009**, *5*, 138.

[53] G. Seo, G. Lee, M. J. Kim, S.-H. Baek, M. Choi, K. B. Ku, C.-S. Lee, S. Jun, D. Park, H. G. Kim, S.-J. Kim, J.-O. Lee, B. T. Kim, E. C. Park, S. I. Kim, *ACS Nano* **2020**, *14*, 5135-5142.

[54] M. Abe, K. Murata, A. Kojima, Y. Ifuku, M. Shimizu, T. Ataka, K. Matsumoto, *J. Phys. Chem. C* **2007**, *111*, 8667-8670.

[55] X. Duan, Y. Li, N. K. Rajan, D. A. Routenberg, Y. Modis, M. A. Reed, *Nat. Nano.* **2012**, *7*, 401-7.

[56] W. Wang, Y. Yang, S. Wang, V. J. Nagaraj, Q. Liu, J. Wu, N. Tao, *Nat. Chem.* **2012**, *4*, 846-853.

[57] X. Duan, Y. Li, N. K. Rajan, D. A. Routenberg, Y. Modis, M. A. Reed, *Nat. Nano.* **2012**, *7*, 401-407.

[58] S. Xu, J. Zhan, B. Man, S. Jiang, W. Yue, S. Gao, C. Guo, H. Liu, Z. Li, J. Wang, Y. Zhou, *Nat. Commun.* **2017**, *8*, 14902.

[59] L. Xie, Y. Yao, Y. Ying, *Appl. Spectrosc. Rev.* **2014**, *49*, 448-461.

[60] N. M. Green, in *Advances in Protein Chemistry*, Vol. 29 (Eds: C. B. Anfinsen, J. T. Edsall, F. M. Richards), Academic Press, 1975, 85-133.

[61] N. M. Green, in *Methods in Enzymology*, Vol. 184 (Eds: M. Wilchek, E. A. Bayer), Academic Press, 1990, 51-67.

[62] B. Qiao, M. Olvera de la Cruz, *ACS Nano* **2020**, *14*, 10616-10623.

[63] R. Lu, X. Zhao, J. Li, P. Niu, B. Yang, H. Wu, W. Wang, H. Song, B. Huang, N. Zhu, Y. Bi, X. Ma, F. Zhan, L. Wang, T. Hu, H. Zhou, Z. Hu, W. Zhou, L. Zhao, J. Chen, Y. Meng, J. Wang, Y. Lin, J. Yuan, Z. Xie, J. Ma, W. J. Liu, D. Wang, W. Xu, E. C. Holmes, G. F. Gao, G. Wu, W. Chen, W. Shi, W. Tan, *The Lancet* **2020**, *395*, 565-574.

[64] D. W. Tholen, K. Linnet, M. Kondratovich, D. A. Armbruster, P. E. Garrett, R. L. Jones, M. H. Kroll, R. M. Lequin, T. J. Pankratz, G. Scassellati, *Protocols for determination of limits of detection and limits of quantitation; approved guideline*, Vol. 24, Clinical and Laboratory Standards Institute, Wayne, Pennsylvania 2004.

[65] A. D. McNaught, U. i. d. c. p. e. appliquée, A. Wilkinson, A. D. Jenkins, I. U. o. Pure, A. Chemistry, *IUPAC Compendium of Chemical Terminology: The Gold Book*, International Union of Pure and Applied Chemistry, 2006.

[66] A. C. Walls, Y.-J. Park, M. A. Tortorici, A. Wall, A. T. McGuire, D. Veesler, *Cell* **2020**, *181*, 281-292.e6.

[67] J. G. Labram, N. D. Treat, Y.-H. Lin, C. H. Burgess, M. A. McLachlan, T. D. Anthopoulos, *Adv. Funct. Mater.* **2016**, *26*, 1656-1663.

[68] J. G. Labram, Y.-H. Lin, K. Zhao, R. Li, S. R. Thomas, J. Semple, M. Androulidaki, L. Sygellou, M. McLachlan, E. Stratakis, A. Amassian, T. D. Anthopoulos, *Adv. Funct. Mater.* **2015**, *25*, 1727-1736.

[69] D. Khim, Y.-H. Lin, S. Nam, H. Faber, K. Tetzner, R. Li, Q. Zhang, J. Li, X. Zhang, T. D. Anthopoulos, *Adv. Mater.* **2017**, *29*, 1605837.

Supporting Information
Supporting Information is available from the Wiley Online Library or from the author.

Acknowledgements
The authors would like to thank Prof. Arnab Pain, as well as Olga Douvropoulou and Raushan Nugmanova from the Biological and Environmental Science and Engineering Division at KAUST (Saudi Arabia) for fruitful discussion and assistance with the materials related to the coronavirus spike protein sensing, and Dr Cheng Sheng Lin from Pitotech Co. Ltd (Taiwan) for useful suggestion and assistance in device modelling and simulation. P.P. and A.D.M. would like to acknowledge the postdoctoral funding for A.D.M. from Vidyasirimedhi Institute of Science and Technology (VISTEC). T.D.A. A.S., A.S., W.A., and H.F. acknowledge support by the King Abdullah University of Science and Technology (KAUST) Office of Sponsored Research (OSR) under awards no. OSR-2018-CARF/CCF-3079 and OSR-CRG2018-3783.

Received: ((will be filled in by the editorial staff))
Revised: ((will be filled in by the editorial staff))
Published online: ((will be filled in by the editorial staff))

ToC Entry: A solution-processed metal oxide heterojunction channel with a geometrically engineered tri-channel architecture several millimetres in size is developed and used as a generic platform for robust, selective and ultra-sensitive detection of various biomolecules. As a proof-of-concept, selective sensing of the SARS-CoV-2 spike protein down to attomolar concentrations in under 2 minutes, is demonstrated.

Authors: Yen-Hung Lin, Yang Han, Abhinav Sharma, Wejdan S. AlGhamdi, Chien-Hao Liu, Tzu-Hsuan Chang, Xi-Wen Xiao, Wei-Zhi Lin, Po-Yu Lu, Akmaral Seitkhan, Alexander D. Mottram, Pichaya Pattanasattayavong, Hendrik Faber, Martin Heeney, Thomas D. Anthopoulos

Title: A tri-channel oxide transistor concept for the rapid detection of biomolecules including the SARS-CoV-2 spike protein

ToC

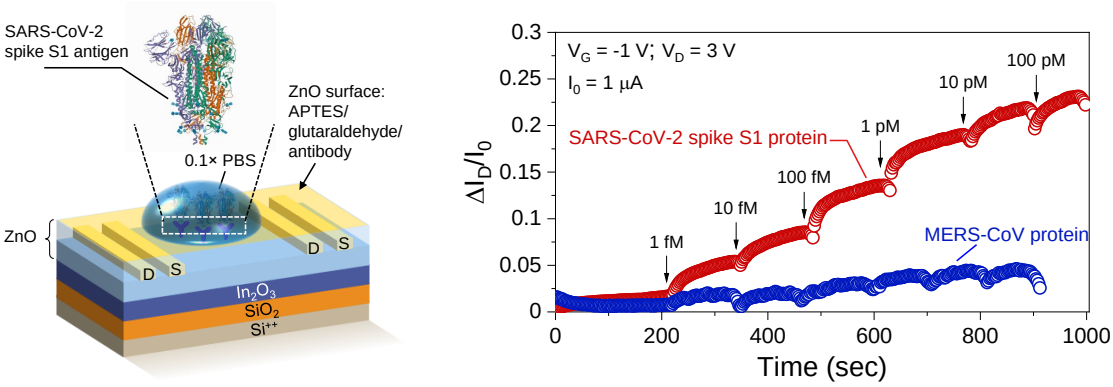

Supporting Information

A tri-channel oxide transistor concept for the rapid detection of biomolecules including the SARS-CoV-2 spike protein

Yen-Hung Lin, Yang Han, Abhinav Sharma, Wejdan S. AlGhamdi, Chien-Hao Liu, Tzu-Hsuan Chang, Xi-Wen Xiao, Wei-Zhi Lin, Po-Yu Lu, Akmaral Seitkhan, Alexander D. Mottram, Pichaya Pattanasattayavong, Hendrik Faber, Martin Heeney*, Thomas D. Anthopoulos**

Correspondence to:
yen-hung.lin@physics.ox.ac.uk
m.heeney@imperial.ac.uk
thomas.anthopoulos@kaust.edu.sa

Supporting Information Text

Experimental and design details of the tri-channel transistor

The channel material for making a tri-channel transistor sensor is based on a modified In_2O_3/ZnO heterostructure. As-cleaned Si/SiO_2 substrates were first deposited with an ultrathin-layer of In_2O_3, followed by the deposition of a ZnO layer (see **Figure S2** step 1-5). The fabrication protocols for preparing In_2O_3/ZnO precursor solutions and their depositions are the same as detailed in the Methods. The source-drain (S-D) electrodes were then formed onto these oxide double layers through thermal evaporation of 30-nm Al (**Figure S2** step 6). To complete this modified In_2O_3/ZnO heterostructure, we first diluted the ZnO precursor (10 mg/mL in ammonium hydroxide) with isopropanol (IPA) to a concentration of 6 mg/mL and followed a similar ZnO deposition protocol (except for thermal annealing at 120 °C for 10 min) to form a layer of ZnO on top of the whole device area (**Figure S2** step 7-8). The half-completed device was functionalised with 1-pyrenebutyric acid (PBA) through a self-assembly process by immersing the device in a PBA-containing solution for 30 min, followed by a thorough washing process with tetrahydrofuran (THF) and a brief post-annealing step for ~5 min at 50-60 °C (**Figure S2** step 9~10). The same self-assembly process was then carried out for the formation of the butyric acid (BA) passivation layer (**Figure S2** step 11-12). The preparation for the PBA and BA solution are detailed in the Methods. Regarding the sensing demonstration of biotin-avidin, the biotin functionalisation was carried out using the same self-assembly procedure as that for the PBA and BA formation. The exact design of our tri-channel transistor sensor is depicted in **Figure S4**. The device is composed of four individual electrode fingers that together form three different channel areas. The sensing part sits right at the centre of the device with a square footprint spanning 4 mm^2 (2 mm by 2 mm) whilst two conventional transistor channels are located on both sides of the sensing area with a channel width of 1,800 μm and a channel length of 100 μm.

Impact on transconductance upon analyte exposure

The transconductance, g_m, of a transistor is given by

$$g_m = \left.\frac{\partial I_D}{\partial V_G}\right|_{V_D} \quad \text{(SI-1)}$$

which is the rate of change of I_D with respect to V_G. The transconductance entails several characteristics of the device: charge transport (mobility), capacitive coupling (geometric gate capacitance), geometrical factor (channel width and length), and operational parameters (gate and drain voltages). The complex geometry of the tri-channel transistor sensor coupled with the In_2O_3/ZnO HJ with quasi two-dimensional (q2D) charge distribution in the channel render the accurate analysis of carrier mobility difficult. In the following, we examine if g_m is suitable for comparing the sensing performance, in particular when all sensors were based on an identical structure and operated under the same parameters.

The plots of transfer characteristics of tri-channel transistor sensors when exposed to (AT)20, A20, and T20 analytes on linear scale are shown in **Figure S14**, **A** to **C** (i.e., **Figure 4**, **B** to **D**, in the main text but plotted on a linear scale). Linear relationships between I_D and V_G especially at high V_G can be observed in all three plots. Since the devices were operated at V_D = 3V, we fit a linear function to each of the transfer curves over a V_G range of 20 V to 30 V. Ensuring that $V_D < V_G - V_{ON}$, i.e. the channel is in the linear regime, the slope of the fit is therefore the average linear-regime transconductance. Their normalized values are plotted in **Figure S14D** to compare the changes in the transport properties as a function of analyte concentrations. As can be observed, the transconductance of the device increases with increasing (AT)20 and A20 concentrations. On the other hand, the transconductance decreases with that of T20, which may be due to Coulomb scattering.[1] However, the difference in g_m for sensing A20 and T20 is highly doubtful to signify the sensitivity of our device as there are no known specific surface interactions or intercalations that would occur between pyrene and ssDNA. We note that although $\Delta I_D/g_m$ has been reported for the estimation of molecules adsorbed,[2] the fact is that g_m highly depends on what the 'regime' a transistor is operated on (e.g. deep-subthreshold, subthreshold, super-subthreshold, etc.) as well as how g_m is extracted. Besides, g_m is a parameter that requires calculation and cannot be output during measurement, hence much less valuable for direct generation of sensing data. Compared to the absolute current level, i.e., I_D, g_m is a device parameter far less suitable for the interpretation of the sensing performance of a transistor sensor, and the bottom line is that a transistor needs to possess an adequate g_m level to generate a perceivable change for signal distinguishability.

Responsivity and sensitivity for biochemical sensing

We introduce two figures of merit: biochemical analyte responsivity ($R_{analyte}$) and analyte sensitivity ($S_{analyte}$) [3]. The $R_{analyte}$ is defined as the change in the channel current upon exposure to a specific analyte concentration [I_D(conc.) in relation to its initial baseline I_D level, i.e. I_D(init.)], and is given as

$$R_{analyte} = \frac{I_D(conc.) - I_D(init.)}{M(conc.)} \quad \text{(SI-2)}$$

where I_D(init.) and I_D(conc.) are the drain current at a specific gate voltage before and after exposure to the analyte at each concentration, while M(conc.) is the analyte molar concentration. The $R_{analyte}$ (in amperes per molar or $A \cdot M^{-1}$) represents the output/input ratio defined as the gain of the sensor and provides information on the extent by which the response of the biosensor changes with varying analyte concentrations. **Figure S15A** shows the evolution of $R_{analyte}$ with V_G for A20, T20 and (AT)20 at different concentrations. For all analytes, the $R_{analyte}$ increases with increasing V_G, due to the transistor's intrinsic current amplification characteristics. The highest and lowest $R_{analyte}$ values are measured for the sensors exposed to (AT)20 and T20, respectively. Of particular interest is the extraordinary value of $R_{analyte}$ ($>10^{10}$ $A \cdot M^{-1}$) measured for the lowest concentrations of (AT)20, indicating that even at 100 aM the sensor is capable of inducing a change in current on the order of μA which can be easily

detected. In some instances the value of $R_{analyte}$ decreases with increasing V_G due to the sensing drain current [I_D(conc.)] approaching the initial channel current level [I_D(init.)]. This effect could be due to changes in the electric field distribution and electrostatic landscape upon changing the gate bias that may affect the surface interactions. Nevertheless, the sensor can be operated at different V_G where the responsivity remains finite, demonstrating the operational versatility of employing a transistor as a sensing platform.

Although $R_{analyte}$ indicates gain, it does not account for the practicalities of operation. A sensor measures the change in signal above a baseline. The larger the background signal, the less accurate the signal measurement becomes. The analyte sensitivity $S_{analyte}$ provides a figure of merit that accounts for this by considering the change in current normalised to the background signal (i.e., initial current):

$$S_{analyte} = \frac{I_D(\text{conc.}) - I_D(\text{init.})}{I_D(\text{init.})}. \quad \text{(SI-3)}$$

In other words, the $S_{analyte}$ provides a measure for the sensor's reaction to the analyte by comparing the increase in the I_D to the baseline current. **Figure S15B** presents the $S_{analyte}$ versus applied V_G and highlights the disparity in the sensor's response to A20, T20 and (AT)20. The dsDNA induces the largest response with a maximum value of 24,000. This extraordinary level of sensitivity is roughly five orders of magnitude larger than the values achieved in those state-of-the-art transistor sensors for comparable analyte concentrations.[4-5] Irrespective of analyte, the $S_{analyte}$ versus V_G plots appear almost identical exhibiting a peak at around $V_G = V_{ON}$(init.).

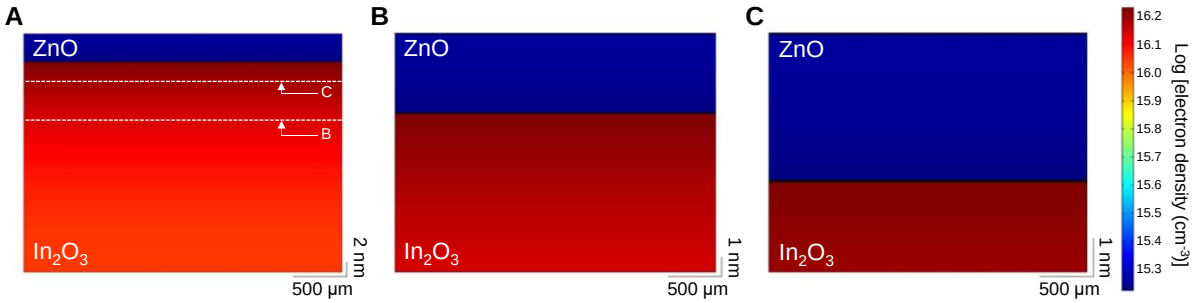

Figure S1. Electron density distribution of In_2O_3/ZnO hetero-oxide structures. Modelling parameters, such as Fermi levels, are taken from our previous works[6-7] with In_2O_3 of different thicknesses (**A**) 30 nm, (**B**) 10 nm (**C**) 3 nm whilst the thickness of ZnO = 5 nm remains the same for all the conditions. Dashed lines B and C shown in (A) represent the relevant positions for (B) and (C), respectively.

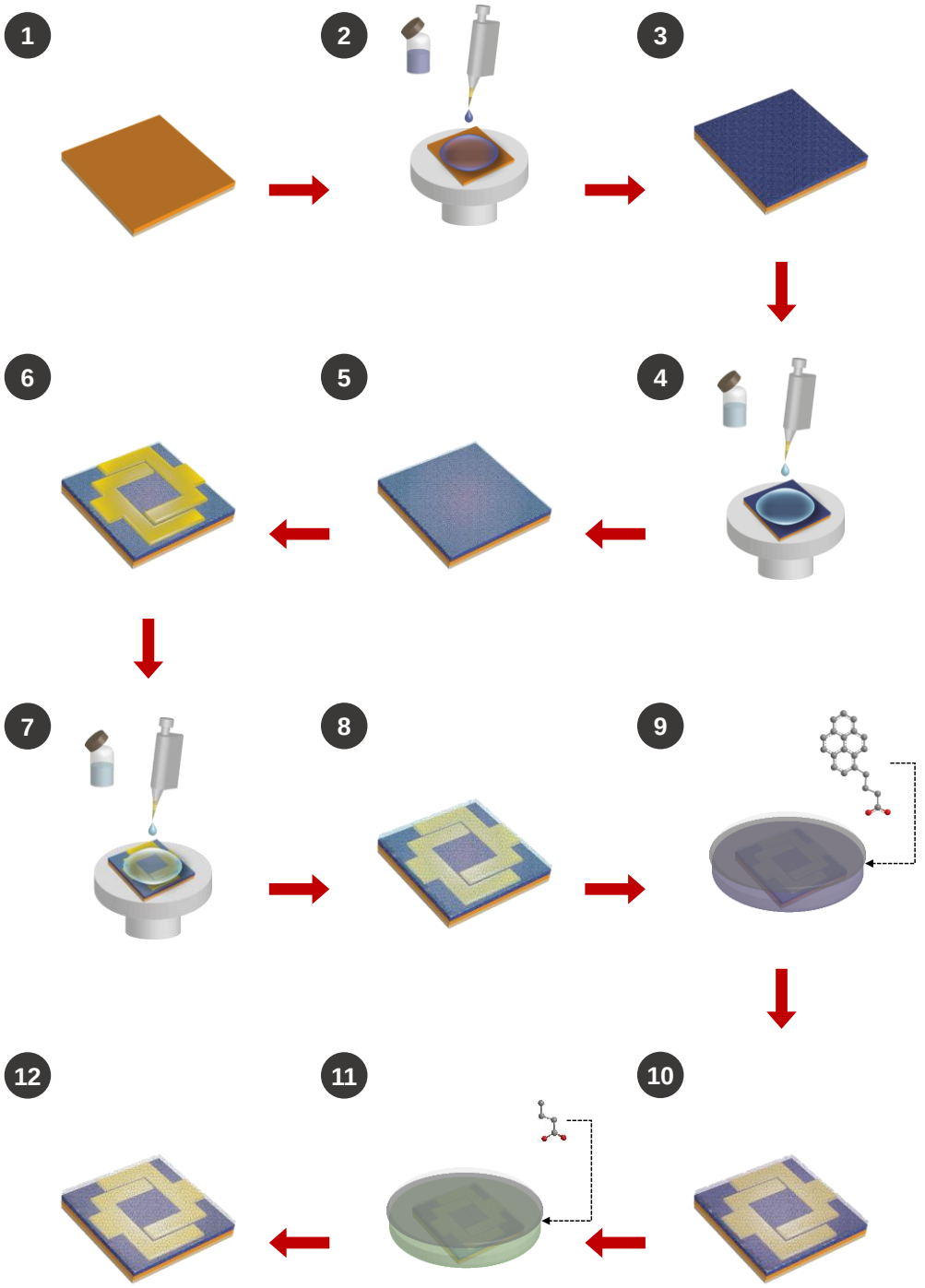

Figure S2. Fabrication process of tri-channel transistor sensor. Schematic of the fabrication process: 1-3) deposition and formation of the bottom In_2O_3 layer onto a Si/SiO_2 substrate; 4-5) deposition and formation of the 1st ZnO layer; 6) Al top electrodes deposition; 7-8) deposition and formation of the 2nd ZnO layer; 9) PBA SAM formation; 10-11) BA SAM formation; 12) complete device.

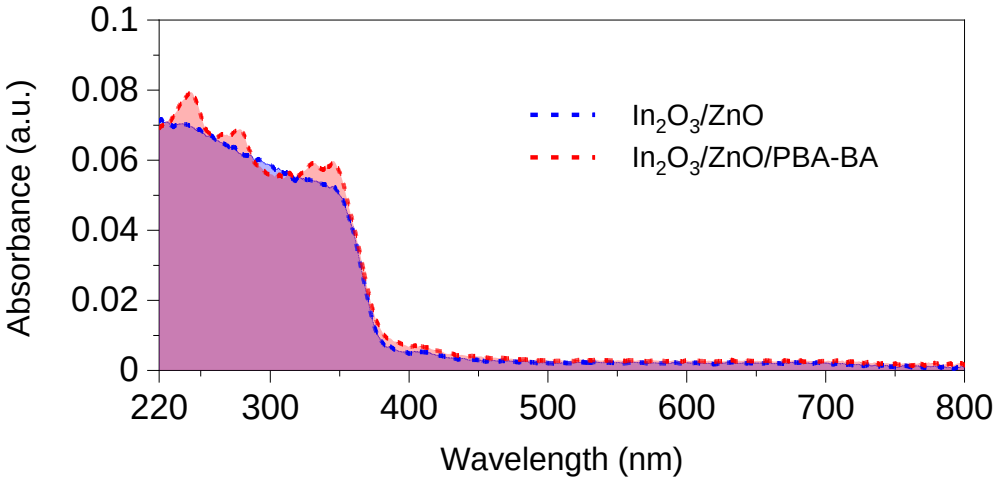

Figure S3. Ultraviolet–visible absorption spectrum. UV-Vis absorption measurements taken for the intrinsic In_2O_3/ZnO hetero film stacks before and after applying the PBA and BA self-assembly processes.

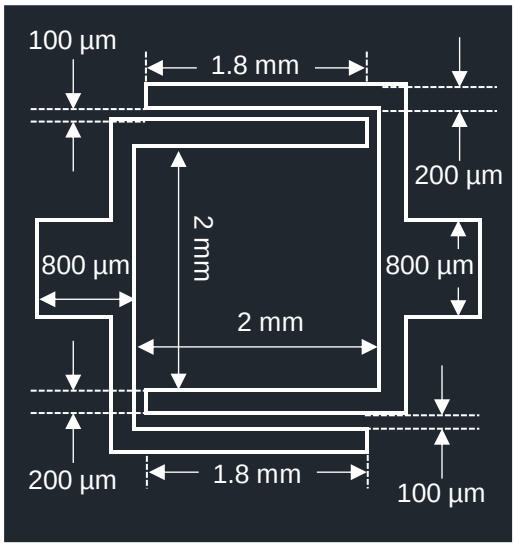

Figure S4. Design of tri-channel transistor sensor. A tri-channel transistor sensor composed of three individual channels: 1) one sensing channel with a square footprint spanning 2 mm by 2 mm in the centre; 2) two identical conventional transistor channels on the sides with a channel width/length of 1,800/100 µm/µm.

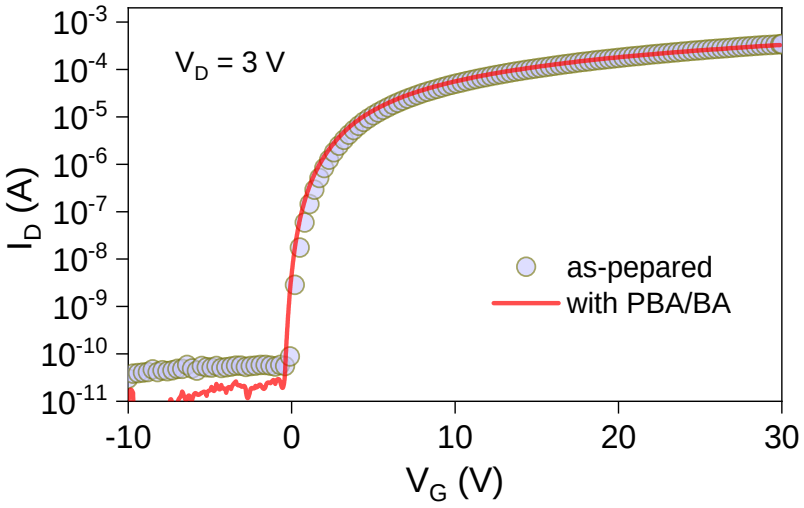

Figure S5. Transfer characteristics before/after SAM functionalisation. Transfer current-voltage (I-V) characteristics of a tri-channel transistor sensor measured as fabricated and after functionalization of the PBA and BA via self-assembly.

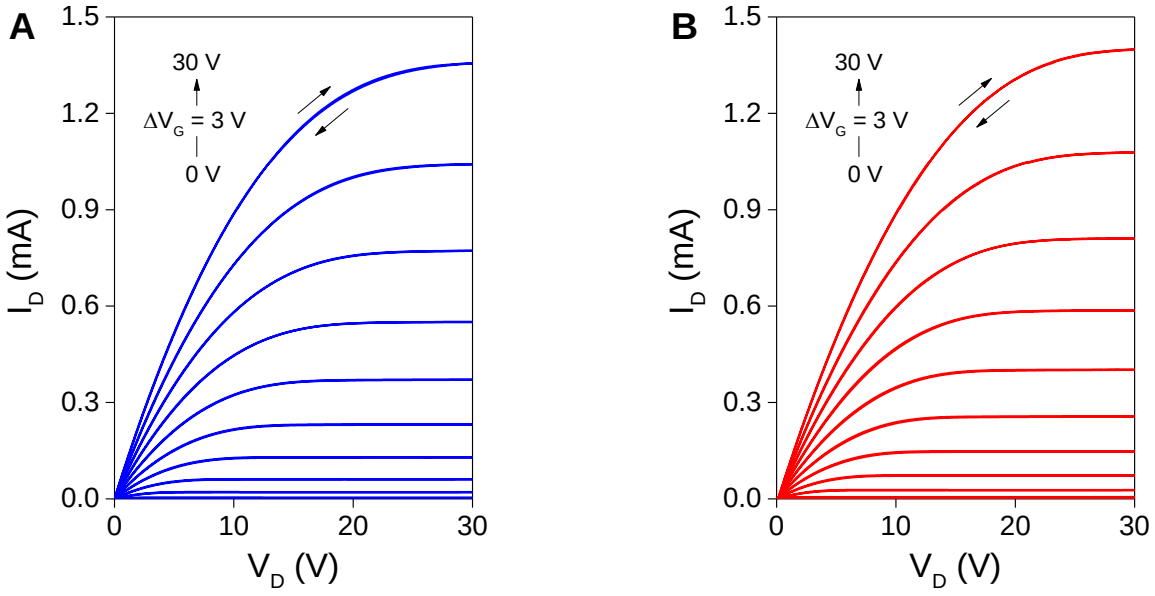

Figure S6. Output characteristics before/after SAM functionalisation. (**A** and **B**) Output current-voltage (I-V) characteristics of a tri-channel transistor sensor measured (A) as fabricated and (B) after the PBA/BA self-assembly processes.

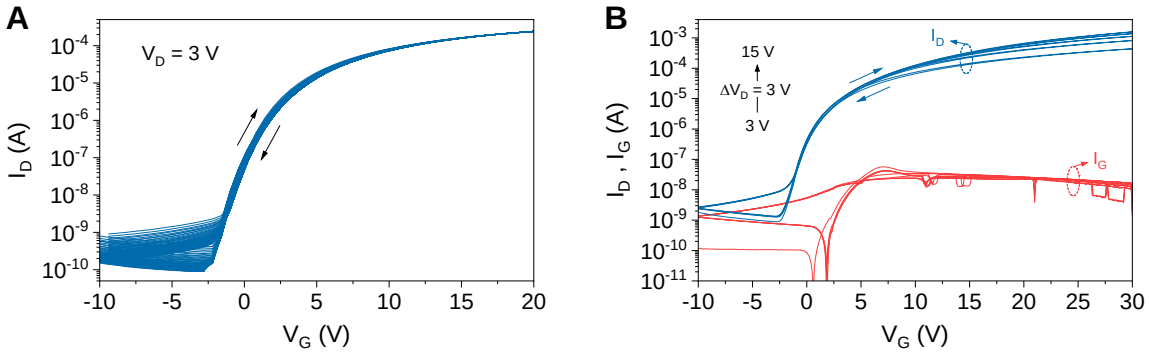

Figure S7. Repeated transfer characteristics and gate leakage current. (**A**) Representative 90 forward-backward dual sweeps of transfer I-V characteristics measured from a tri-channel transistor. (**B**) A typical set of transfer characterisation results for a tri-channel transistor sensor exhibits negligible contribution from gate leakage current to device electrical performance beyond V_{ON}.

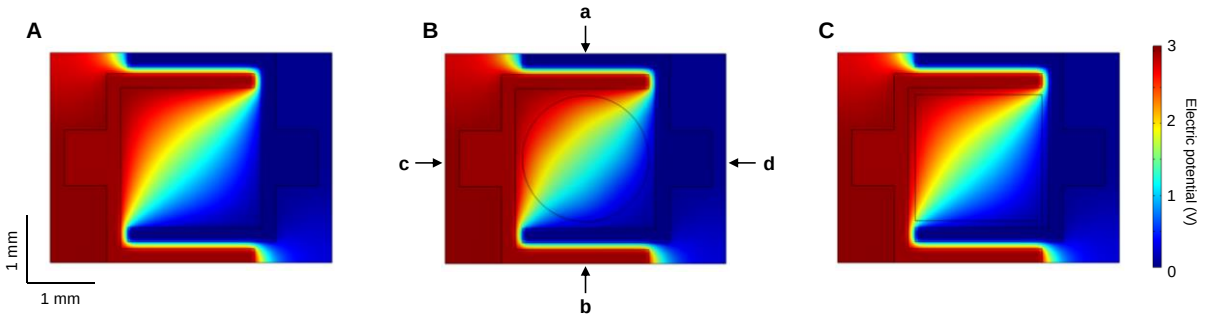

Figure S8. Top view of electric potential in In_2O_3 tri-channel transistors. Devices under a static state condition of V_G = 8 V and V_D = 3 V: (**A**) without any analyte, (**B**) with a circular-shaped analyte (diameter = 1.8 mm, surface charge density = 3.3×10^9 cm^{-2}) and (**C**) a square-shaped analyte (side length = 1.8 mm, surface charge density = 3.3×10^9 cm^{-2}). In (B), arrows a and b indicate the position modelled in Figure 3 whilst arrows c and d indicate the direction perpendicular to the a-b plane.

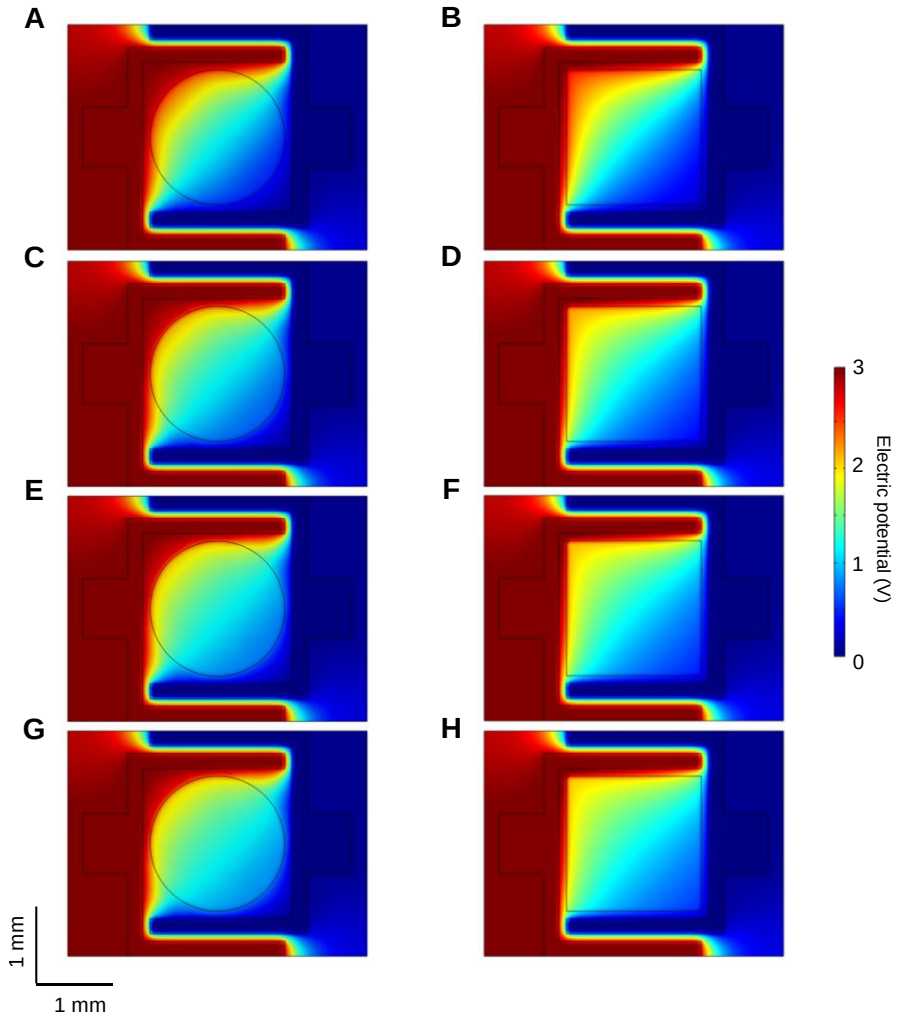

Figure S9. Top view of electric potential with various modelled analytes. In_2O_3 tri-channel transistors under a static state condition of V_G = 8 V and V_D = 3 V with the presence of different surface charge densities as modelled analytes: (**A** and **B**) 1.3×10^{10} cm^{-2}, (**C** and **D**) 3.3×10^{10} cm^{-2}, (**E** and **F**) 5.0×10^{10} cm^{-2} and (**G** and **H**) 6.7×10^{10} cm^{-2}.

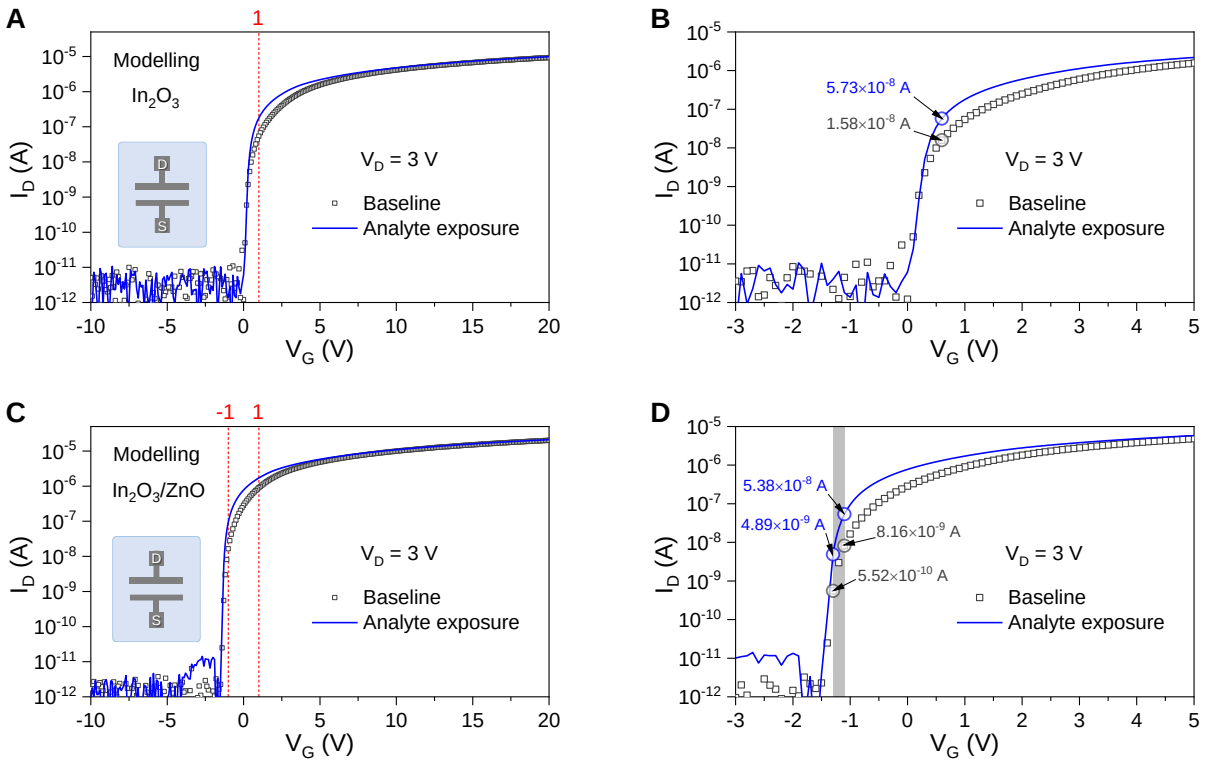

Figure S10. Modelled current-voltage characteristics for a conventional channel architecture. (**A** to **D**) COMSOL modelled transfer current-voltage (I-V) characteristic obtained at V_D = 3 V. Modelled transfer characteristics for transistors based on a single channel layer of In_2O_3 (A and B) and an In_2O_3/ZnO heterojunction (C and D). (A and C) show the full ranges of simulated I-V characteristics whilst (B and D) show the I-V characteristics for V_G in the range -3 to 5 V. When comparing the largest differences in the channel current (ΔI_D) for baseline and exposure to a simulated analyte, the largest $\Delta I_D/I_0$ obtained for In_2O_3/ZnO and In_2O_3 transistors are 7.86 and 2.63, respectively.

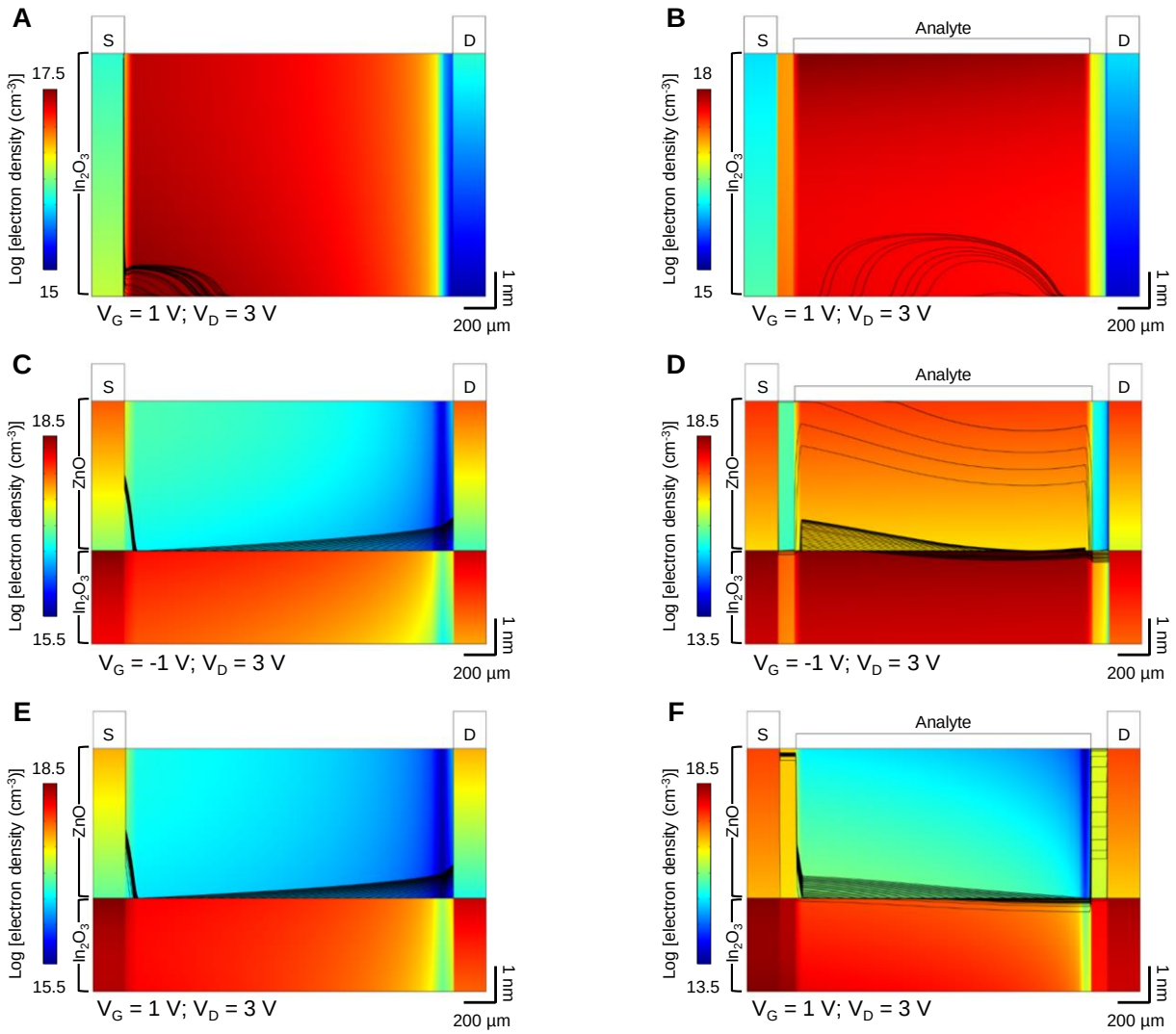

Figure S11. Simulated electron density distributions. (**A** to **F**) COMSOL modelled electron density distributions and electron flow streamlines (all under V_D = 3 V) for baseline: (A) In_2O_3 (V_G = 1 V), (C) In_2O_3/ZnO (V_G = -1 V) and (E) In_2O_3/ZnO (V_G = 1 V); and under the exposure of simulated analytes (B) In_2O_3 (V_G = 1 V), (D) In_2O_3/ZnO (V_G = -1 V) and (F) In_2O_3/ZnO (V_G = 1 V). The electrodes and analytes are shown to indicate their positions with respect to the devices.

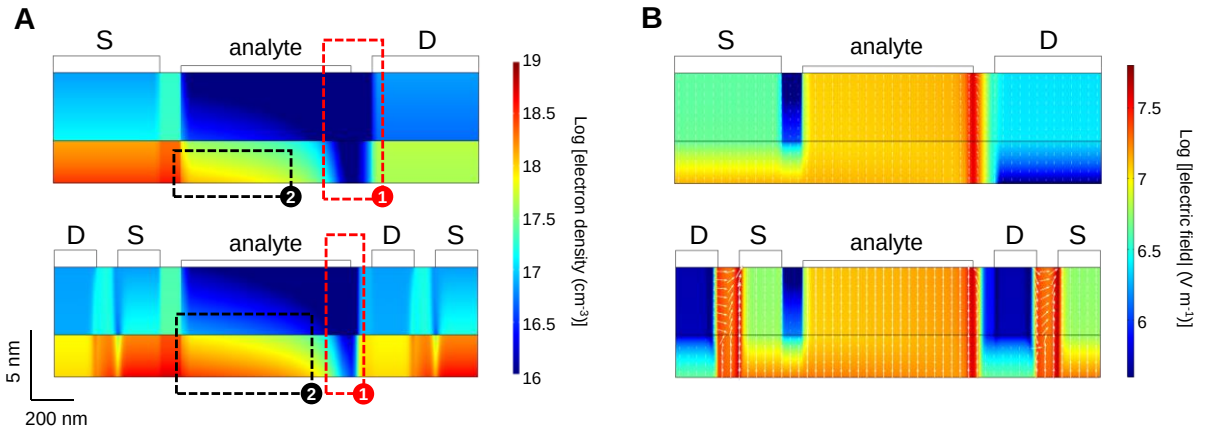

Figure S12. Comparisons of carrier densities and electric fields between the conventional single channel and the tri-channel device designs. (**A**) Electron density distribution under V_G = 3 V and V_D = 3 V with the presence of modelled analytes using a surface charge density of 5×10^9 cm^{-2}. (**B**) Corresponding electric field distributions, where arrows indicate the direction of electric fields, and the length of each arrow represents the electric-field intensity.

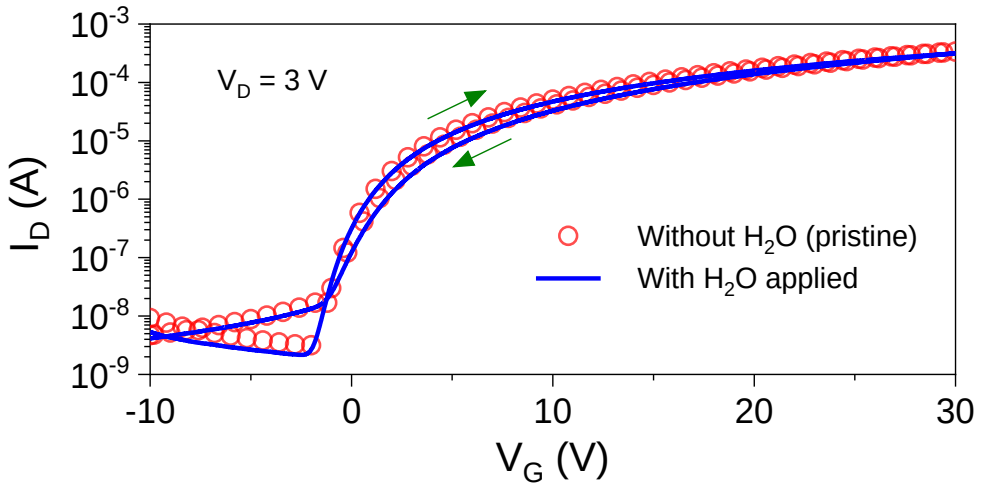

Figure S13. Transfer characteristics of a tri-channel transistor sensor under the presence of H_2O. Transfer I-V characterisation for a tri-channel transistor sensor carried out with H_2O present on the device sensing area. There is virtually no change in the key performance parameters: as for the initial state, V_{ON} = -2.0 V, I_{ON} = 0.32 mA, S.S. = 0.72 V/dec; and under the presence of H_2O, V_{ON} = -2.1 V, I_{ON} = 0.32 mA, S.S. = 0.73 V/dec.

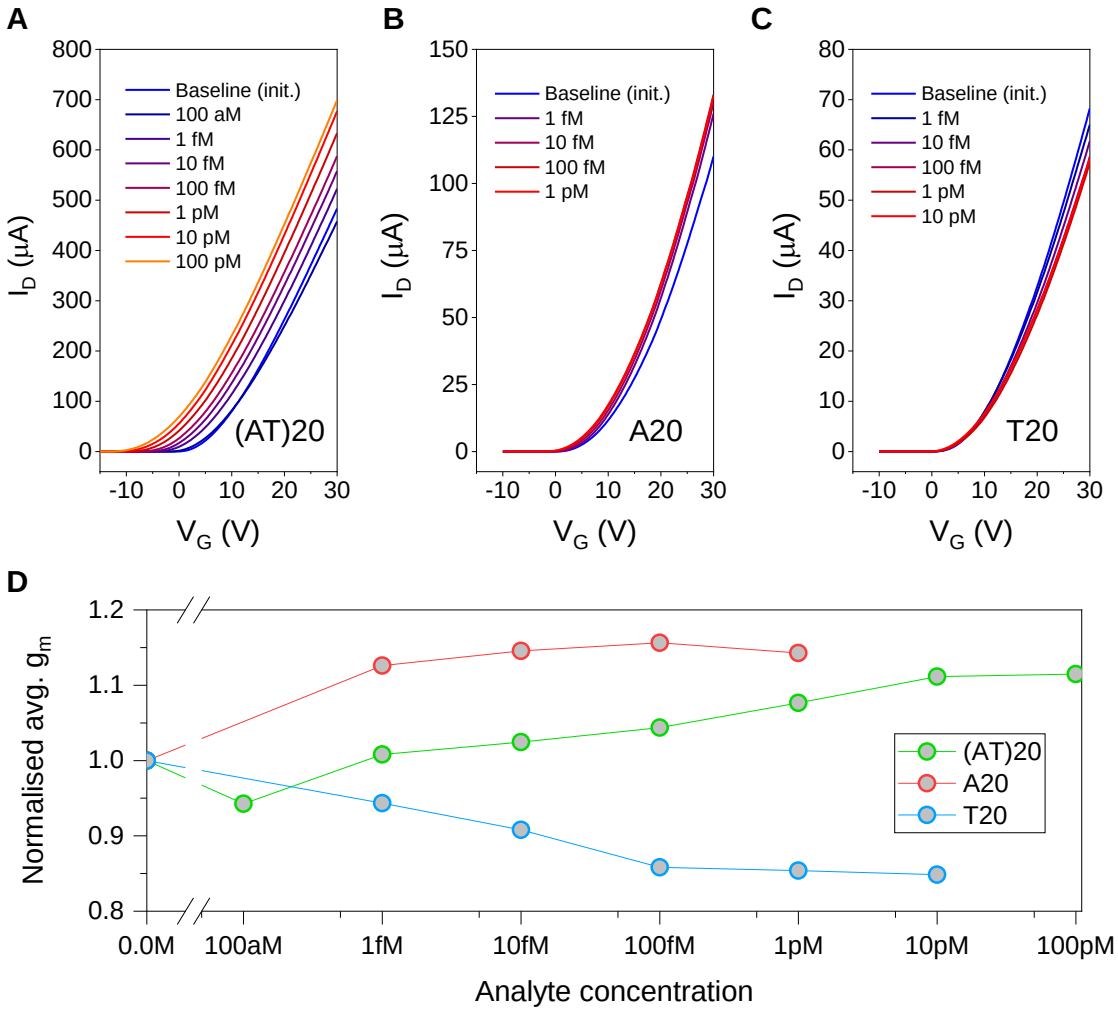

Figure S14. Linear transfer characteristics and transconductance. (**A** to **C**) Plots of I_D vs. V_G in linear scale of tri-channel transistor sensors at various concentrations of: (A) (AT)20, (B) A20, and (C) T20. The linear relationship particularly at high V_G shows that the devices operate in the linear regime. (**D**) Average linear transconductance of the plots in (a)-(c) calculated from the slope of the linear portion in the range V_G = 20-30 V. The values are normalised to the initial baseline values (no analyte).

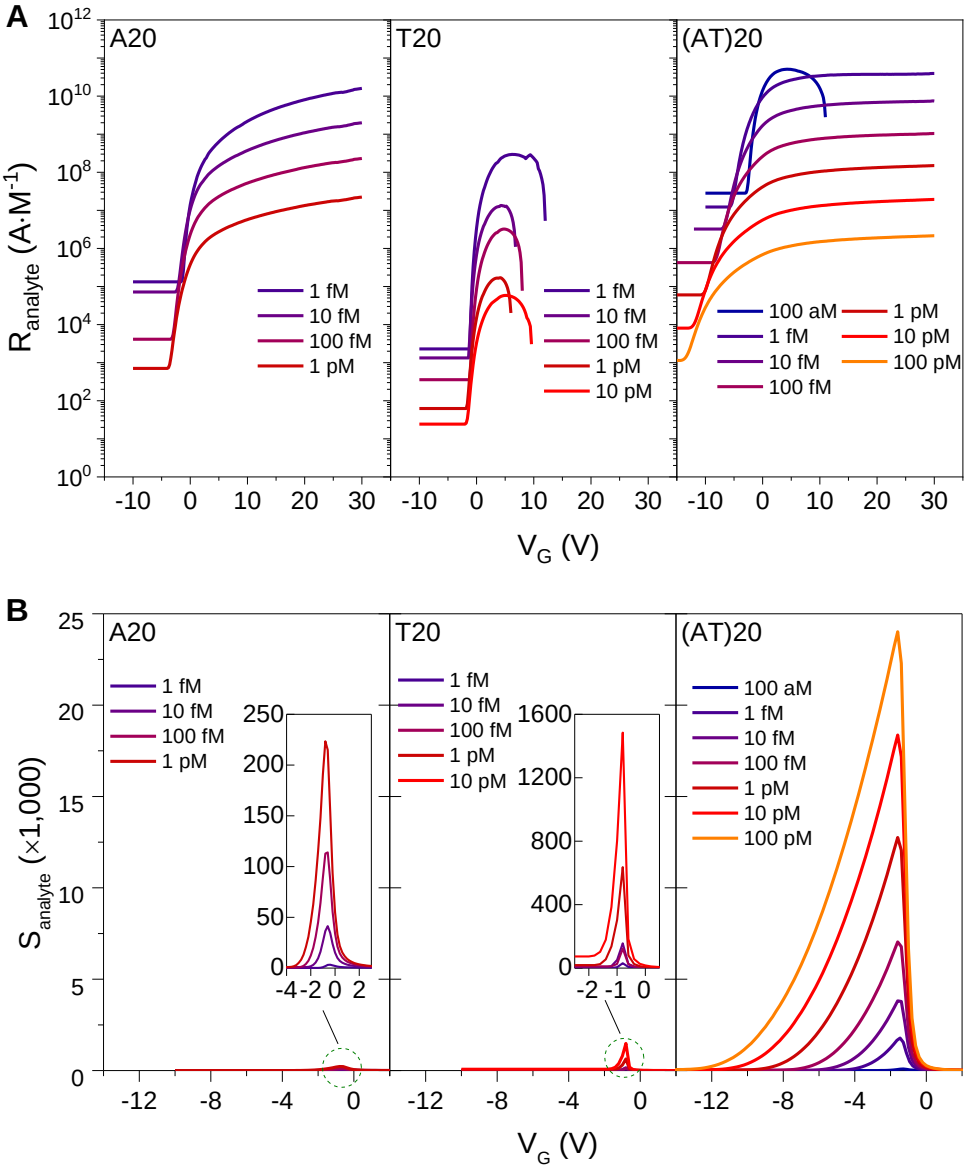

Figure S15. Evaluation of the tri-channel transistor sensor performance. (**A**) Plots of analyte responsivity $R_{analyte}$ versus applied gate voltage for the different analyte DNAs studied at various concentrations. $R_{analyte}$ represents the V_G-dependent output/input signal gain of the biochemical-sensing. (**B**) Plots of the analyte sensitivity $S_{analyte}$ as a function of gate voltage for the different DNA analytes at different concentrations. $S_{analyte}$ represents the signal-to-noise ratio.

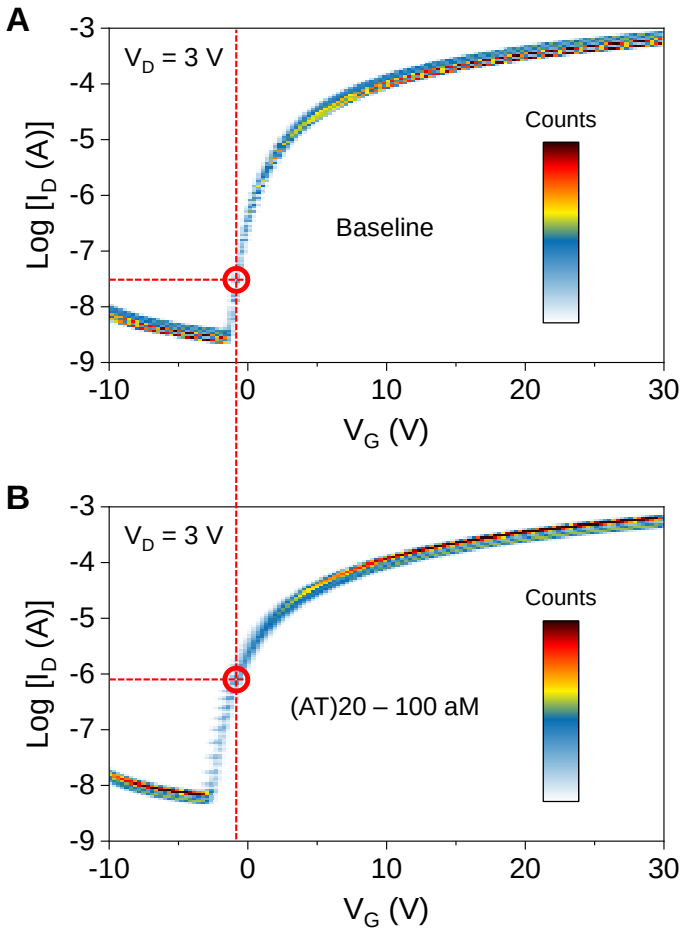

Figure S16. Transfer characteristics without and with the presence of (AT)20. Density plots of transfer I-V characteristics measured from 8 individual tri-channel transistors for (A) baseline and under (B) 100 aM of (AT)20. Red dashed lines indicate the I_D levels at V_G = -1 V.

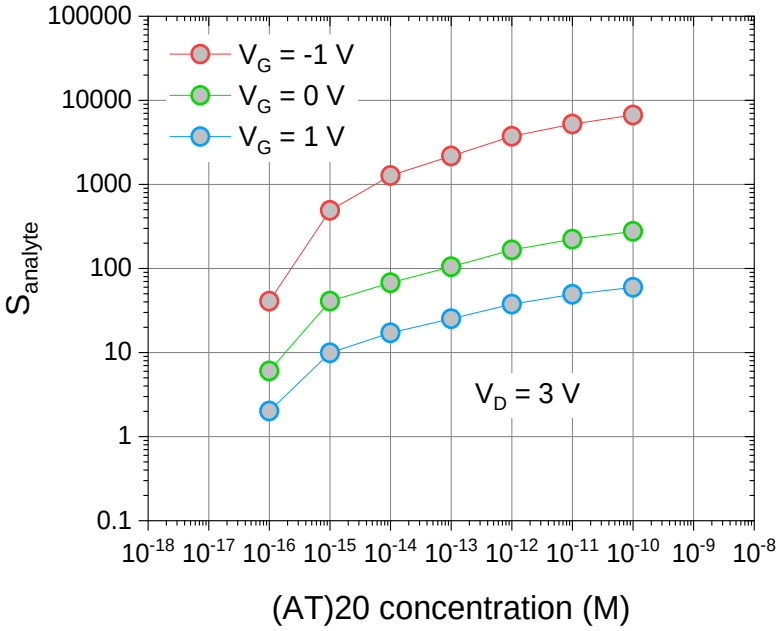

Figure S17. Analyte sensitivity for (AT)20 in different operating regimes. Plots of $S_{analyte}$ vs (AT)20 at a range of concentrations from 100 aM to 100 pM when operating a tri-channel transistor sensor at V_D = 3 V and V_G = -1 V (red), 0 V (green) and 1 V (blue). Higher $S_{analyte}$ achieved from biasing at V_G = -1 V is a result of the low initial/baseline channel current I_D. When operating at V_G = 1 V, the increase in the initial I_D level reduces the distinguishable margin in I_D for the lowest analyte concentration (i.e., 100 aM). However, one should also note that even though the lowest $S_{analyte}$ value of ~2 measured from the biasing condition of V_D = 3 V and V_G = 1 V, our solid-state tri-channel transistor sensor still outperforms current state-of-the-art transistor sensors reported in the literature using electrochemical approaches at similar analyte concentrations.[4-5]

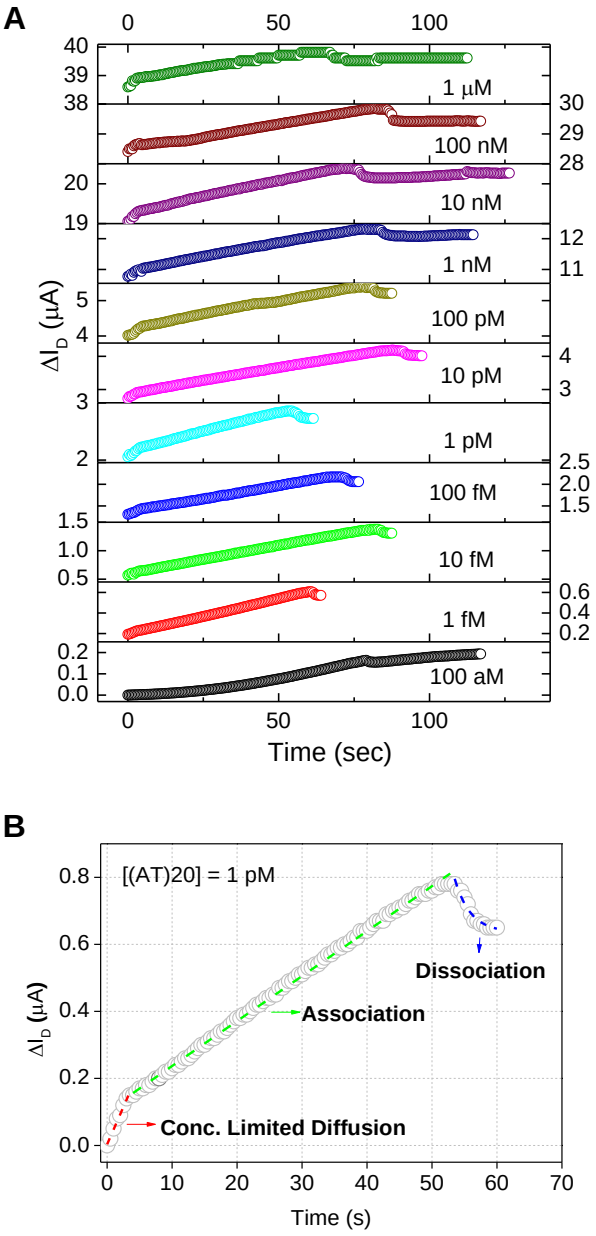

Figure S18. Time course of the sensing process of (AT)20. (**A**) Monotonic increase in channel current at different (AT)20 concentrations. (**B**) An example time course at [(AT)20] = 1 pM. The entire sensing process can be divided into three steps: a short time concentration-limited diffusion (the diffusion is faster when a higher (AT)20 concentration is applied); the association of (AT)20 with pyrene moieties on the surface of the sensor device via intercalation (the main sensing step, a zero-order reaction); and the dissociation of the formed complex until a thermal dynamic equilibrium is reached. The concentration-limited diffusion was fitted with a linear model: $y = 0.000344 + 0.00461x$ ($R^2 = 0.985$). The zero-order association step was fitted based on a linear model of $y = 0.0107 + 0.0014x$ ($R^2 = 0.998$). The dissociation step was fitted according to an exponential decay: $y = 0.0653 + 0.0163 \times \exp[-(x-53.5) / 2.65]$ ($R^2 = 1.00$).

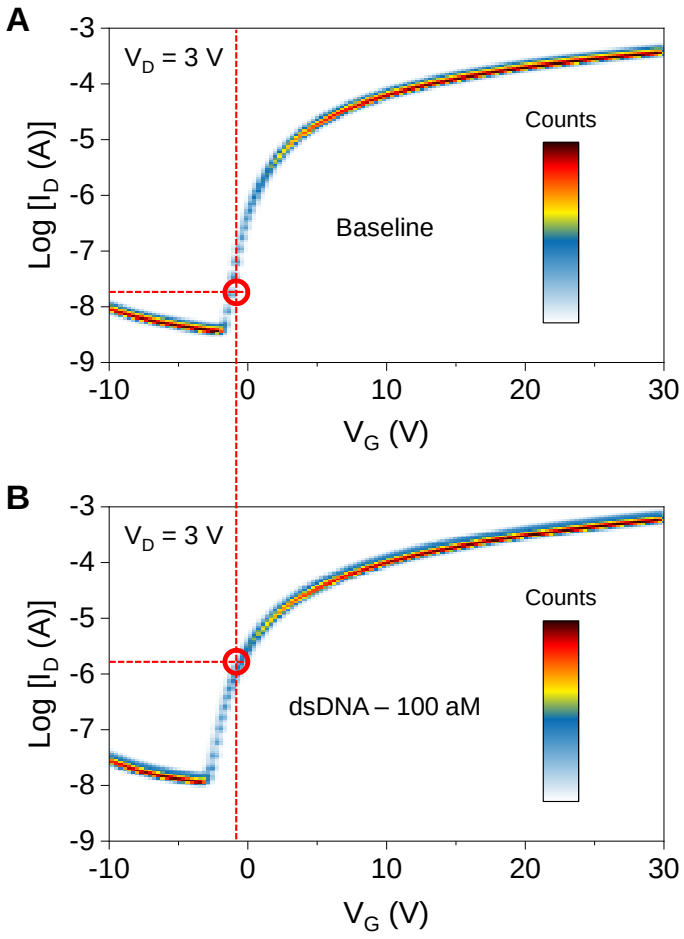

Figure S19. Transfer characteristics without/with natural dsDNA. Density plots of transfer I-V characteristics measured from 8 individual tri-channel transistors for (A) baseline and under (B) 100 aM of natural dsDNA. Red dashed lines indicate the I_D levels at V_G = -1 V.

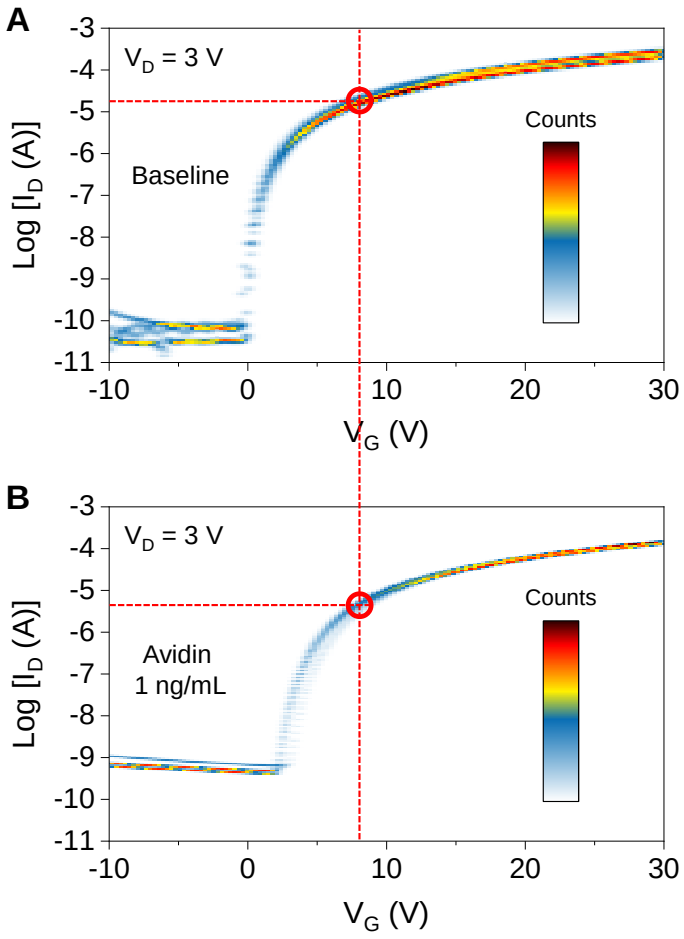

Figure S20. Transfer characteristics without/with the presence of avidin. Density plots of transfer I-V characteristics measured from 8 individual tri-channel transistors for (A) baseline and under (B) 1 ng/mL of avidin. Red dashed lines indicate the I_D levels at V_G = 8 V.

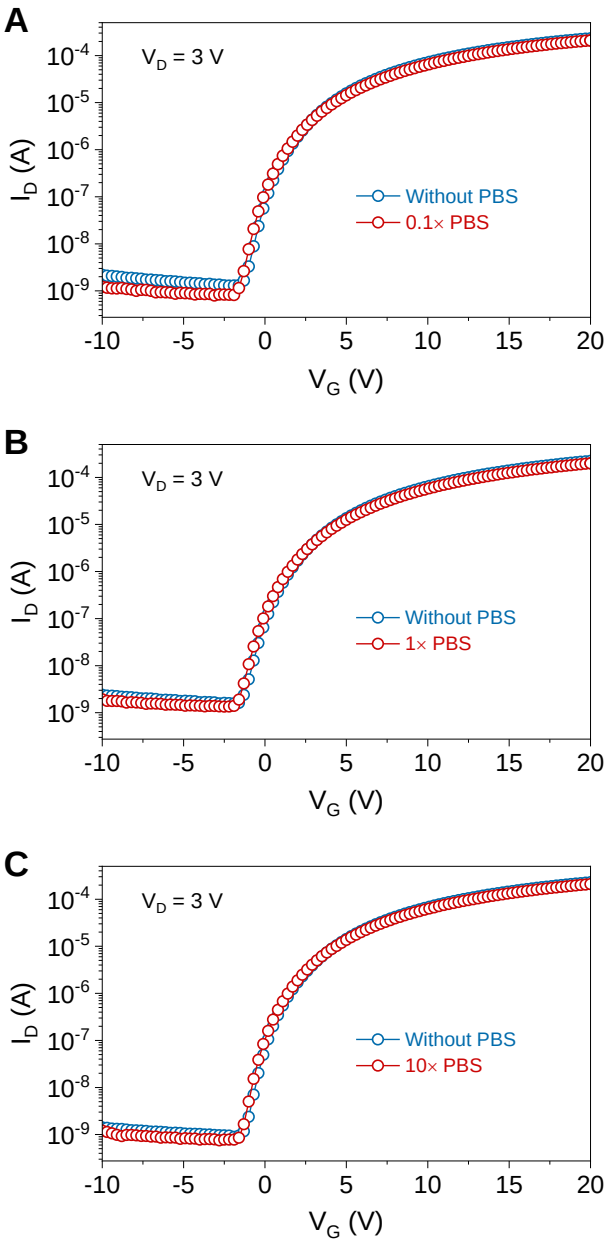

Figure S21. Transfer characteristics without/with the presence of PBS. Representative transfer I-V characteristics of tri-channel transistor sensors measured without and with the presence of (A) 0.1× PBS; (B) 1× PBS; (C) 10× PBS.

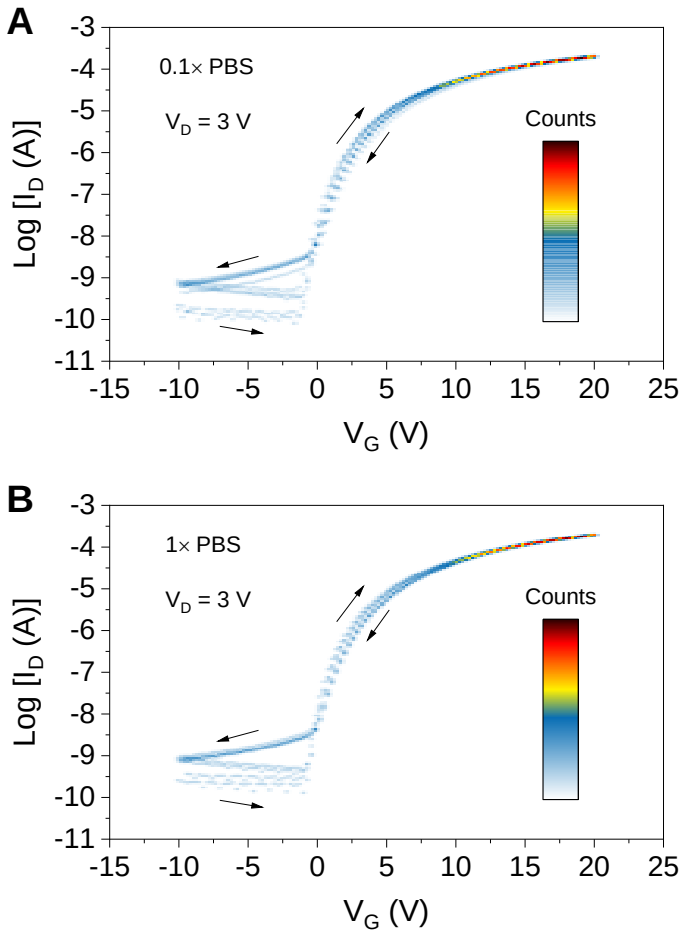

Figure S22. Transfer characteristics under the presence of PBS. Density plots of 5 sets of transfer I-V characteristics from tri-channel transistors under (A) 0.1× and (B) 1× PBS.

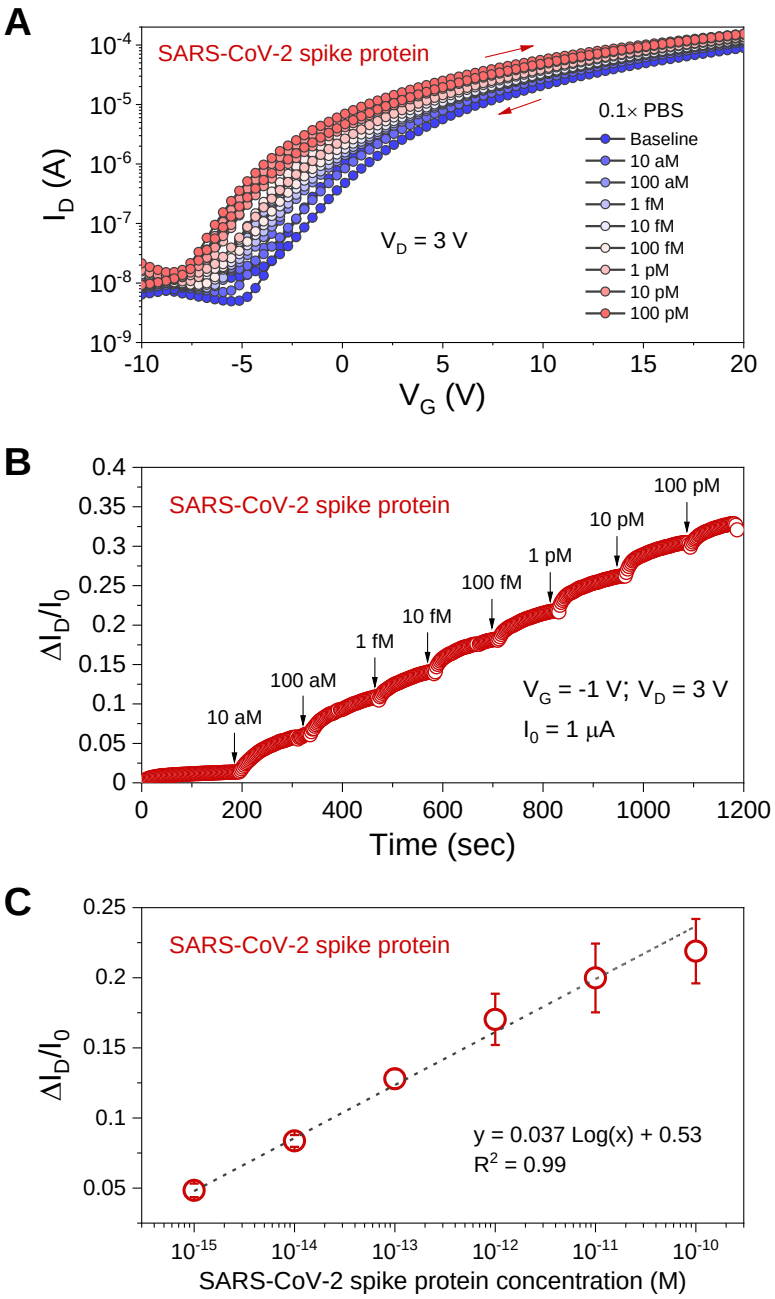

Figure S23. Detection of SARS-CoV-2 spike protein. (**A**) Dual-sweep transfer I-V characteristics for a tri-channel transistor sensor subjected to a series of SARS-CoV-2 spike protein concentrations in 0.1× PBS (baseline). (**B**) Representative real-time detection of SARS-CoV-2 spike protein in 0.1× PBS. (**C**) Corresponding calibration plot from (B). The error bars denote standard deviations from three real-time measurement sets. The limit of detection of 865 aM was estimated from 3 S_b/m, where S_b is the standard deviation of the measurements for blank PBS-only solution, and m is the slope of the calibration curve.[8]

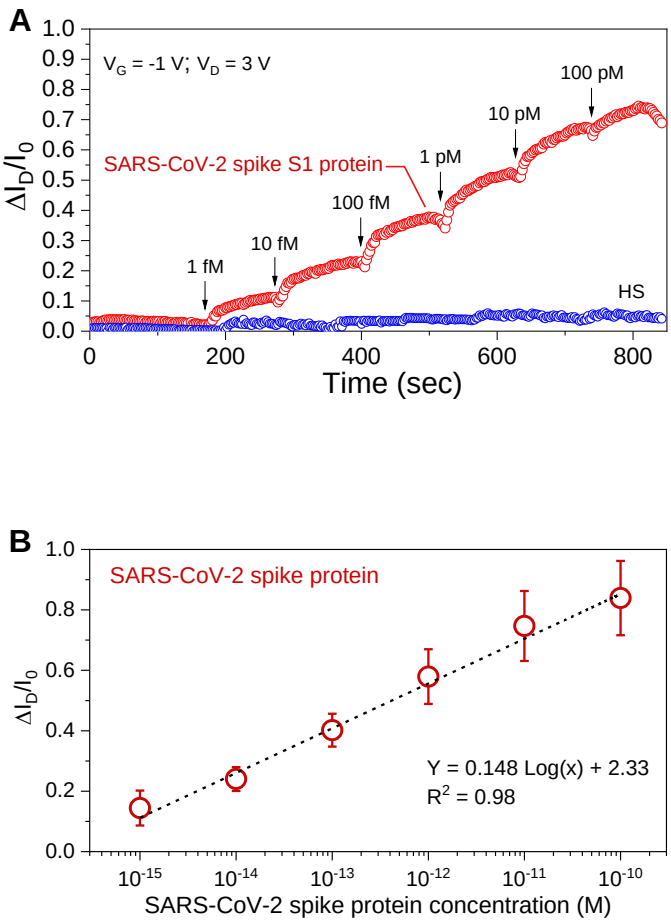

Figure S24. Detection of SARS-CoV-2 spike protein in human serum. (**A**) A representative set of real-time detection of SARS-CoV-2 spike S1 protein at a range of concentrations in 10-fold human serum (HS). (**B**) Corresponding calibration plot with the error bars denoting standard deviations from three (n = 3) real-time measurement sets.

Supporting Information References

[1] S. P. Schießl, H. Faber, Y.-H. Lin, S. Rossbauer, Q. Wang, K. Zhao, A. Amassian, J. Zaumseil, T. D. Anthopoulos, *Adv. Mater.* **2016**, *28*, 3952-3959.

[2] X. Duan, Y. Li, N. K. Rajan, D. A. Routenberg, Y. Modis, M. A. Reed, *Nat. Nano.* **2012**, *7*, 401-407.

[3] G. Konstantatos, M. Badioli, L. Gaudreau, J. Osmond, M. Bernechea, F. P. G. de Arquer, F. Gatti, F. H. L. Koppens, *Nat. Nano.* **2012**, *7*, 363.

[4] E. Macchia, K. Manoli, B. Holzer, C. Di Franco, M. Ghittorelli, F. Torricelli, D. Alberga, G. F. Mangiatordi, G. Palazzo, G. Scamarcio, L. Torsi, *Nat. Commun.* **2018**, *9*, 3223.

[5] N. Nakatsuka, K.-A. Yang, J. M. Abendroth, K. Cheung, X. Xu, H. Yang, C. Zhao, B. Zhu, Y. S. Rim, Y. Yang, P. S. Weiss, M. N. Stojanović, A. M. Andrews, *Science* **2018**.

[6] H. Faber, S. Das, Y.-H. Lin, N. Pliatsikas, K. Zhao, T. Kehagias, G. Dimitrakopulos, A. Amassian, P. A. Patsalas, T. D. Anthopoulos, *Sci. Adv.* **2017**, *3*, e1602640.

[7] Y.-H. Lin, W. Li, H. Faber, A. Seitkhan, N. A. Hastas, D. Khim, Q. Zhang, X. Zhang, N. Pliatsikas, L. Tsetseris, P. A. Patsalas, D. D. C. Bradley, W. Huang, T. D. Anthopoulos, *Nat. Electron.* **2019**, *2*, 587-595.

[8] D. W. Tholen, K. Linnet, M. Kondratovich, D. A. Armbruster, P. E. Garrett, R. L. Jones, M. H. Kroll, R. M. Lequin, T. J. Pankratz, G. Scassellati, *Protocols for determination of limits of detection and limits of quantitation; approved guideline*, Vol. 24, Clinical and Laboratory Standards Institute, Wayne, Pennsylvania 2004.